Rolling resistance of a rigid sphere with viscoelastic coatings

Gérard-Philippe Zéhil[a,*], Henri P. Gavin[a]

[a]*Department of Civil and Environmental Engineering, Duke University, 121 Hudson Hall, Box 90287, Research Drive, Durham, NC 27708-0287, United States*

Abstract

We present a novel three-dimensional boundary-element formulation that fully characterizes the mechanical behavior of the external boundary of a multi-layered viscoelastic coating attached to a hard rotating spherical core. The proposed formulation incorporates both, the viscoelastic, and the inertial effects of the steady-state rolling motion of the sphere, including the Coriolis effect. The proposed formulation is based on Fourier-domain expressions of all mechanical governing equations. It relates two-dimensional Fourier series expansions of surface displacements and stresses, which results in the formation of a compliance matrix for the outer boundary of the deformable coating, discretized into nodes. The computational cost of building such a compliance matrix is optimized, based on configurational similarities and symmetry. The proposed formulation is applied, in combination with a rolling contact solving strategy, to evaluate the viscoelastic rolling friction of a coated sphere on a rigid plane. Steady-state results generated by the proposed model are verified by comparison to those obtained from running dynamic simulations on a three-dimensional finite element model, beyond the transient. A detailed application example includes a verification of convergence and illustrates the dependence of rolling resistance on the applied load, the thickness of the coating, and the rolling velocity.

Keywords: Rolling resistance, coated sphere, viscoelastic layers, boundary element method, Fourier series.

1. Introduction and background

Viscoelasticity is a time-dependent model of material behavior capable of replicating the storage and restitution (elasticity), and the dissipation in the bulk at different internal rates (viscosity), of variable proportions of the deformation energy. Particles and solids of rounded shape presenting viscoelastic properties, or interacting mechanically with other viscoelastic entities, with or without direct contact, are involved in many aspects of sciences and technologies, in various fields, and at different length-scales, from the smallest fundamental particles (e.g. Berg, 1999), to nano-materials and living cells (e.g. Bahadur and Schwartz, 2008; Bose et al., 2010; Coghill, 2012; Subramaniam et al., 2013; Xu and Shao, 2008), to various sorts of objects and systems at the human scale, such as the motion of rigid spheres in polymer gels (e.g. Hunter, 1968), the vibratory sorting of fruits and vegetables (e.g. Arnold, 1985), polymer-coated grinding spheres (e.g. Langus et al., 2011), rubber bullets (e.g. Bir et al., 2012), particle dampers (e.g. Els, 2009), structural damping fillers (e.g. Oyadiji, 1996), computer mouse-balls, spherical wheels for vehicles and robots (e.g. Wu and Hwang, 2008; Wu et al., 2011), flows of viscoelastic fluids around spheres (e.g. Atsbha, 1993), flows of granular materials (e.g. Yung et al., 2007; Zhou et al., 1999), human or animal joints (e.g. Esat and Ozada, 2010), and rolling balls in seismic isolation platforms (e.g. Harvey and Gavin, 2013; Harvey et al., 2013; Tsai et al., 2010), to the largest planets, and stars (e.g. Bambusi and Haus, 2012).

Among all possible types of static or dynamic interactions between one, two, a few, or even very large numbers of rounded entities, those involving contact are very common, and often accompanied by losses of mechanical energy. Upon rolling or sliding, mechanical energy is transformed into heat in the continuum of those of the interacting objects that are characterized by a viscoelastic behavior. This dissipative process in the bulk, known as viscoelastic "rolling

*Corresponding author
Email address: gerard.zehil@duke.edu (Gérard-Philippe Zéhil)

resistance", or viscoelastic "rolling friction", is reflected by changes in the mechanical fields (i.e. the stresses and strains) across the contact interfaces, so as to resist the ongoing motion.

Problems related to the resistance incurred by rigid indenters, such as cylinders, spheres and cones, rolling or sliding on a viscoelastic plane, are addressed quite extensively in the scientific literature, both experimentally and from a modeling perspective, in two and three dimensions, and at different scales, such as in the works of Bueche and Flom (1959); Carbone and Putignano (2013); Chertok et al. (2001); Flom and Bueche (1959); Flom (1960); Galin and Gladwell (2008); Greenwood and Tabor (1958); Greenwood et al. (1961); Hunter (1961); Johnson (1985); Lee et al. (2009); May et al. (1959); Persson (2010); Pöschel et al. (1999); Qiu (2006); Tabor (1952, 1955); Zéhil and Gavin (2013c,a,b), to cite a few. Alternatively, the rolling contact between viscoelastic cylinders, or between a viscoelastic cylinder and a rigid plane is analyzed for instance by Golden and Graham (2001); Kumar et al. (1988); Morland (1967, 1968); Munisamy et al. (1991); Nowell and Hills (1988); Oden and Lin (1986); Qiu (2009); Wang and Knothe (1993), while Hall (2001) presents a nice review of the fundamentals of rolling resistance from the perspective of the tire industry. However, quite surprisingly, problems involving the rolling/sliding friction of viscoelastic spheres have received far less attention. In the following, we briefly review four studies that focus on the rolling resistance incurred by a *solid* viscoelastic sphere on a rigid plane, mostly, in narrow ranges of the parameters.

Brilliantov and Pöschel (1998) propose an approximate closed-form expression for the friction coefficient of a solid viscoelastic sphere of radius R rolling on a hard plane, in quasi-static conditions and under small deformations. The authors assume that the characteristic time of the motion, defined as the ratio of the sphere's deformation $d = R-H$ (H being the distance between the center of the deformed sphere and the contact surface) to its rolling velocity V_s, is much larger than the material's internal time scales τ_k. In agreement with this regime of motion and with the small strain assumption $d/R \ll 1$, inertial forces are neglected and the vertical displacement field is approximated by the corresponding result of the stationary contact problem, as given by Hertz (1881). The behavioral characterization of the viscoelastic material is limited to two viscous parameters, or equivalently, to a single relaxation time for each of the shear modulus and the bulk modulus. In fact, the stress field is written as the sum of an elastic part $\boldsymbol{\sigma}_e$, and a viscous part $\boldsymbol{\sigma}_v$, which corresponds to the Kelvin-Voigt model, characterized by a constant storage modulus, and by a loss modulus increasing linearly with frequency. This choice is consistent with the other assumptions retained by the authors in the sense that the linearization of any frequency-domain viscoelastic master-curves about zero frequency, corresponds to a Kelvin-Voigt model. This fact is readily inferred, for instance, from their equations (65a) and (65b). It is assumed that the elastic part of the contact stress field is almost unaffected by the (slow) motion, and that it remains roughly symmetrical. Its contribution to the resisting torque T_r is hence neglected, in comparison to that of the viscous stress field. The authors show that, within the framework of the proposed theory, the resisting torque scales linearly with the vertical load applied to the rolling sphere P, with its radius R, its angular speed Ω, and therefore with its velocity $V_s \approx R\Omega$. The proposed expression is however flawed due to an error in a coordinate system transformation, as recently determined by Zheng et al. (2011).

A few years later, Yung and Xu (2003) argue that, in most practical cases, the material's internal rates of dissipation cannot be considered much smaller than the characteristic time of motion, and therefore conclude that more accurate expressions are needed for the rolling resistance of viscoelastic spheres, which take into account the "influence of relaxation". To this aim, the authors 'relax' the assumption $d/V_s \gg \tau_k$, attempting to reveal the nonlinear dependence of rolling resistance on velocity, at moderately higher rates of motion. They however stipulate, for simplicity, that the fields in the continuum of the sphere, at a given cycle, are not influenced by the preceding cycles, which is equivalent to maintaining the limiting condition that $\Omega\tau_k \ll 1$. It is interesting to note that the latter constraint is satisfied implicitly under the assumptions retained earlier by Brilliantov and Pöschel (1998), i.e. $\Omega\tau_k \ll d/R \ll 1$. In contrast, Yung and Xu (2003)'s assumptions that $\Omega\tau_k \ll 1$ and that $d/R \ll 1$ are unconnected, which expands the applicability domain of their theory to the nonlinear regime, by increasing the upper bound on Ω. In deriving a nonlinear relation for rolling resistance, the authors make several other simplifying assumptions, some of which are quite limiting, and somewhat inconsistent with their stated goal, such as retaining one Kelvin-Voigt element to model the material's behavior. Indeed, this material model is characterized by a single rate of internal dissipation and is known to better reflect creep than relaxation. Other approximations include: (i) introducing the viscous behavior vertically and pointwise (ii) neglecting inertial effects under the quasi-static approximation, (iii) retaining the same contact radius r_c and deformation d as the stationary Hertzian solution, (iv) assuming a sinusoidal stress distribution across the contact surface, calibrated to yield the same maximum contact pressure as that of the stationary solution, (v) evaluating an 'average' density of dissipated energy at one point of 'average' position with 'average' values of

	Relevant models: Author (Year)				
Principal model characteristics and main assumptions retained	Brilliantov and Pöschel (1998)	Yung and Xu (2003)	Zheng et al. (2011)	Zheng et al. (2011)	Zéhil and Gavin (2013)
Type of the proposed model	Analytical	Analytical	Analytical	Numerical/FE	Semi-Analytical
Viscoelastic material description retained	Kelvin-Voigt	Kelvin-Voigt	Kelvin-Voigt	Kelvin-Voigt	General
Are inertial effects accounted for?	No	No	No	No	Yes
Is the Coriolis effect accounted for?	No	No	No	No	Yes
Does the model support surface frictions?	No	No	No	No	Yes
Can the model handle coated spheres?	No	No	No	No	Yes
Does the model support multiple layers?	No	No	No	No	Yes
Is a contact solving strategy proposed?	No	No	No	FE/ABAQUS	Yes
Are stationary contact fields retained?	Yes	Yes	Yes	Partially	No
Is the contribution $\boldsymbol{\sigma}_e$ to T_r neglected?	Yes	Yes	Yes	Yes	No
Does the model rely on: $\Omega\tau_k \ll d/R$?	Yes	Yes	Yes	Yes	No
Does the model rely on: $d/R \ll 1$?	Yes	Yes	Yes	Yes	Partially
Does the model rely on: $\Omega\tau_k \ll 1$?	Yes	Yes	Yes	Yes	No

Table 1: Comparison between the semi-analytical model proposed in this work and previous relevant works addressing the rolling resistance of *solid* viscoelastic spheres: principal model characteristics and main assumptions retained.

the fields, and (vi) evaluating the total dissipation by integration over a "deformed volume" $2\pi R r_c d$ of ring-like cross section defined by the contact path $2\pi R$, the 'average' contact width r_c, and the deformation d. The resulting analytical expression for rolling resistance is quite cumbersome. A numerical example reveals that, according to the proposed theory, rolling friction first increases, then decreases, with increasing velocity. However, given the constitutive model retained, and in the absence of inertial effects, the physical mechanisms causing the rolling friction to decrease with increasing speed is rather unclear.

Xu et al. (2007) present an experimental apparatus that measures the steady-state coefficient of rolling friction $T_r/(PR)$ of a squash ball on a conveyor belt, at moderate velocities. The setup was designed to fill an identified gap in the availability of accessible methods to perform rolling resistance experiments involving deformable spheres. It was later used in a classroom for teaching purposes. The different sources of power dissipation contributing to rolling resistance cannot be clearly distinguished using the proposed device. Indeed, energy losses occur not only in the bulk of the sphere, but also to some extent in the bulk of the deformable conveyor belt, and at the contact interface in case of slipping friction as well. Nevertheless, the experimental results presented by the authors, for the combined losses, confirm the linear dependence of the coefficient of rolling friction on the translational velocity V_s, at moderate rates of motion.

More recently, Zheng et al. (2011) implement, using the commercial software ABAQUS, a finite element (FE) model for the steady-state rolling resistance of a solid viscoelastic sphere on a rigid plane, under the quasi-static approximation. The material's behavior is characterized as in the work of Brilliantov and Pöschel (1998), with the additional assumption that the viscous parameter associated with the bulk modulus is equal to zero, which in fact corresponds to the three-dimensional formulation of the material behavior retained by Yung and Xu (2003). The FE model's implementation is focused on the regime where $\Omega\tau_k \ll 1$, which corresponds to the elastic part of the contact stress field being much larger than the viscous part, but also to small values of rolling resistance. To avoid that the resisting toque be affected by numerical errors on $\boldsymbol{\sigma}_e$, the authors override the finite element software to compute the resisting torque from $\boldsymbol{\sigma}_v$ only, hence neglecting the contribution of $\boldsymbol{\sigma}_e$. The numerical model is exploited in the conditions corresponding to $\Omega\tau_k \ll d/R$ and to $d/R \ll 1$. In this regime, the coefficient of rolling friction, defined as $T_r/(PR)$, is found to be almost independent from the vertical load P applied to the sphere, and to vary linearly with the rolling speed Ω. The authors also derive an analytical expression for rolling friction, based on the assumptions retained by Brilliantov and Pöschel (1998), which matches the results of their numerical model fairly well.

It is interesting to note that, in the papers discussed above, either (i) a simplified formulation is retained which does not involve a rolling contact problem, or (ii) a more sophisticated numerical approach is adopted, but the resolution of contact is carried out by means of a commercially available tool, with minimal discussion.

To date, no work has ever addressed the modeling (and the solving) of the resistance incurred by a rigid sphere, covered with a viscoelastic coating, rolling or sliding, on a rigid plane. In this work, we present a novel three-dimensional boundary-element formulation that fully characterizes the mechanical behavior of the external boundary

of a multi-layered viscoelastic coating attached to a hard rotating spherical core. A brief comparison between the semi-analytical model proposed in this work and the previous relevant works addressing the rolling friction of solid viscoelastic spheres is presented in table 1. The proposed formulation incorporates both, the viscoelastic, and the inertial effects of the steady-state rolling motion of the sphere, including the Coriolis effect. Linear viscoelastic materials are characterized by frequency-domain master-curves. This choice of material description is the most general in that it accommodates broad-spectrum Prony series with as many internal time-scales as practically needed, as well as fully experimental results from dynamic mechanical analyses, resonant ultrasound spectroscopies, or broadband viscoelastic spectroscopies (e.g. Eakasit et al., 2009; Lakes, 2004, 2009; Lee et al., 2000; Menard, 2008). The proposed formulation takes advantage of the periodicity of all fields in the continuum. It is based on Fourier-domain expressions of local equilibrium equations, constitutive equations and boundary conditions. It relates two-dimensional Fourier series expansions of surface displacements and stresses, which results in the formation of a compliance matrix for the outer boundary of the deformable coating, discretized into nodes. Taking advantage of configurational similarities and symmetry, the computational cost of building compliance matrices is reduced significantly. The proposed formulation may be leveraged in important aspects of the modeling of several types of problems, pertaining to different fields, in various settings and at multiple scales, such as mechanical interactions between nano-particles and/or biological organisms, bone articulations, granular materials, round-shaped components in industrial machineries, in transport vehicles of all kinds, in satellites, in robots, and in risk mitigation devices such as seismic isolation platforms. Furthermore, in the constant improvement process of discrete element models (DEM), which are often used to study the flow of granular materials, such as earth materials in traditional extruders, or plastic pellets in micro-injection moulding machines (e.g Yung et al., 2007), aspects of the proposed formulation may be called upon to account for the viscoelastic rolling friction between particles. An extension of the three-dimensional rolling contact solving strategy proposed by Zéhil and Gavin (2013a), to the case of a deformable sphere rolling/sliding on rigid plane, is also presented in this work. The boundary element model of the coated sphere and the rolling contact algorithm are combined to evaluate the resistance to motion. A detailed application example includes a verification of convergence and illustrates the dependence of rolling friction on the applied load, the thickness of the coating, and the rolling speed.

2. Problem setting

Figure 1 shows a hard spherical core, of radius r_i, coated with a layer of viscoelastic material of uniform thickness $h = r_o - r_i$, which is perfectly bonded to the core. The sphere is considered to be rolling on a rigid plane, in the x-direction, at a constant angular speed Ω. In our most general case, the rolling object is subjected to: (i) a vertical load P acting downwards, (ii) a driving horizontal force Q acting in the direction of motion, and (iii) a driving torque T, acting clockwise. The external actions P, Q and T are applied at point C, at the center of the rolling sphere. The absolute linear velocity of point C is designated by V_s. Due to the deformation of the coating, the distance H between point C and the rigid plane is smaller than the outer radius of the sphere, i.e. $H \leq r_o$.

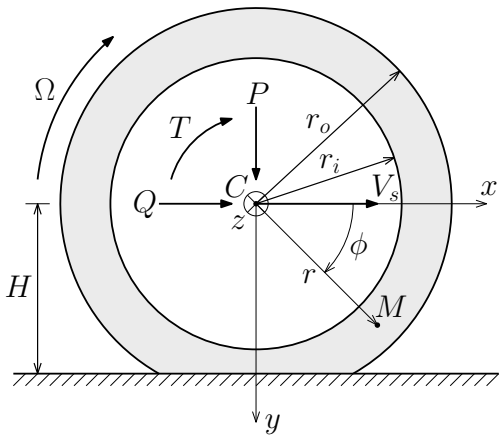

Figure 1: General model of a coated sphere and its coordinate systems.

The moving rectangular coordinate system $Cxyz$ follows point C, without rotating. Let $Cr\phi\theta$ be the spherical coordinate system to which $Cxyz$ is related, according to the set of equations below:

$$x = r\cos(\phi)\sin(\theta); \qquad y = r\sin(\phi)\sin(\theta); \qquad z = r\cos(\theta). \tag{1}$$

The inclination θ is taken from the z-axis, and the azimuthal angle ϕ is the angle from the x-axis about the z-axis. The spherical coordinates r, ϕ and θ can be related to their primed counterparts, rotating with the sphere, by a simple transformation involving the time variable t, i.e.

$$r = r'; \qquad \phi = \phi' + \Omega t; \qquad \theta = \theta'. \tag{2}$$

Because the state of motion is steady, any generic field $f(r,\phi,\theta)$ in the continuum of the coating does not depend explicitly on time. Furthermore, equations (2) lead to a spatial expression of the n^{th}-order derivative of $f(r,\phi,\theta)$ with respect to time

$$\frac{d^n f}{dt^n} = \Omega^n \frac{\partial f}{\partial \phi}. \tag{3}$$

3. Governing equations

Let u_r, u_ϕ and u_θ be the components of the displacement field in $Cr\phi\theta$, along the unit vectors $\mathbf{e}_r$, $\mathbf{e}_\phi$ and $\mathbf{e}_\theta$ respectively. The position vector of a (displaced) point $M(r,\phi,\theta)$ in the continuum writes

$$\mathbf{x}(r,\phi,\theta) = (r+u_r)\,\mathbf{e}_r + u_\phi \mathbf{e}_\phi + u_\theta \mathbf{e}_\theta. \tag{4}$$

The velocity and acceleration fields are obtained by differentiating equation (4) with respect to time, according to expression (3), which yields

$$\mathbf{v}(r,\phi,\theta) = \Omega\left[\left(u_{r,\phi} - u_\phi \sin(\theta)\right)\mathbf{e}_r + \left(u_{\phi,\phi} + (r+u_r)\sin(\theta) + u_\theta\cos(\theta)\right)\mathbf{e}_\phi + \left(u_{\theta,\phi} - u_\phi\cos(\theta)\right)\mathbf{e}_\theta\right], \tag{5}$$

$$\begin{aligned}\mathbf{a}(r,\phi,\theta) = {} & \Omega^2\left(u_{r,\phi\phi} - 2u_{\phi,\phi}\sin(\theta) - (r+u_r)\sin(\theta)^2 - u_\theta\sin(\theta)\cos(\theta)\right)\mathbf{e}_r \\ & + \Omega^2\left(u_{\phi,\phi\phi} - u_\phi + 2u_{r,\phi}\sin(\theta) + 2u_{\theta,\phi}\cos(\theta)\right)\mathbf{e}_\phi \\ & + \Omega^2\left(u_{\theta,\phi\phi} - 2u_{\phi,\phi}\cos(\theta) - (r+u_r)\sin(\theta)\cos(\theta) - u_\theta\cos(\theta)^2\right)\mathbf{e}_\theta.\end{aligned} \tag{6}$$

The local equilibrium equations in the continuum of the layer write

$$\mathbf{div}(\boldsymbol{\sigma}) = \rho\mathbf{a} \tag{7}$$

where $\boldsymbol{\sigma}$ is the stress tensor and ρ is the density of the viscoelastic material. Plugging equation (6) into (7) and expressing (7) in spherical coordinates yields

$$\begin{aligned}&\sigma_{rr,r} + \frac{1}{r}\sigma_{r\theta,\theta} + \frac{1}{r\sin(\theta)}\sigma_{r\phi,\phi} + \frac{1}{r}\left(2\sigma_{rr} - \sigma_{\theta\theta} - \sigma_{\phi\phi} + \sigma_{r\theta}\cot(\theta)\right) = \\ &\qquad \rho\Omega^2\left(u_{r,\phi\phi} - 2u_{\phi,\phi}\sin(\theta) - (r+u_r)\sin(\theta)^2 - u_\theta\sin(\theta)\cos(\theta)\right) \qquad (8a)\\ &\sigma_{r\phi,r} + \frac{1}{r}\sigma_{\theta\phi,\theta} + \frac{1}{r\sin(\theta)}\sigma_{\phi\phi,\phi} + \frac{1}{r}\left(2\sigma_{\theta\phi}\cot(\theta) + 3\sigma_{r\phi}\right) = \\ &\qquad \rho\Omega^2\left(u_{\phi,\phi\phi} - u_\phi + 2u_{r,\phi}\sin(\theta) + 2u_{\theta,\phi}\cos(\theta)\right) \qquad (8b)\\ &\sigma_{r\theta,r} + \frac{1}{r}\sigma_{\theta\theta,\theta} + \frac{1}{r\sin(\theta)}\sigma_{\theta\phi,\phi} + \frac{1}{r}\left(\left(\sigma_{\theta\theta} - \sigma_{\phi\phi}\right)\cot(\theta) + 3\sigma_{r\theta}\right) = \\ &\qquad \rho\Omega^2\left(u_{\theta,\phi\phi} - 2u_{\phi,\phi}\cos(\theta) - (r+u_r)\sin(\theta)\cos(\theta) - u_\theta\cos(\theta)^2\right) \qquad (8c)\end{aligned}$$

It is interesting to note that the term $\rho\Omega^2 r\sin(\theta)^2$ appearing in equation (8a), which is maximum in the xy-plane and decreases laterally, corresponds to the Coriolis effect due to the rotation of the sphere about the z-axis. The components of the strain tensor $\boldsymbol{\epsilon}$ are expressed, in spherical coordinates, in terms of the displacements as follows

$$\epsilon_{rr} = u_{r,r}, \tag{9a}$$

$$\epsilon_{\phi\phi} = \frac{1}{r\sin(\theta)}\left(u_{\phi,\phi} + u_r\sin(\theta) + u_\theta\cos(\theta)\right), \tag{9b}$$

$$\epsilon_{\theta\theta} = \frac{1}{r}\left(u_{\theta,\theta} + u_r\right), \tag{9c}$$

$$\epsilon_{r\phi} = \frac{1}{2}\left(\frac{1}{r\sin(\theta)}u_{r,\phi} + u_{\phi,r} - \frac{1}{r}u_\phi\right), \tag{9d}$$

$$\epsilon_{r\theta} = \frac{1}{2}\left(\frac{1}{r}u_{r,\theta} + u_{\theta,r} - \frac{1}{r}u_\theta\right), \tag{9e}$$

$$\epsilon_{\phi\theta} = \frac{1}{2r}\left(\frac{1}{\sin(\theta)}u_{\theta,\phi} + u_{\phi,\theta} - u_\phi\cot(\theta)\right). \tag{9f}$$

Let $\lambda(t)$ and $\mu(t)$ be the time dependent Lamé parameters characterizing the viscoelastic behavior of the layer's material. Assuming that stresses and strains are equal to zero for all negative values of the time variable t, the constitutive equations of linear isotropic viscoelasticity can be written, using indicial tensor notation, as (Flügge, 1975; Lakes, 2009; Tschoegl, 1989)

$$\sigma_{ij}(t) = \int_{-\infty}^{\infty} 2\mu(t-\tau)\frac{\partial\epsilon_{ij}}{\partial\tau}d\tau + \delta_{ij}\int_{-\infty}^{\infty}\lambda(t-\tau)\frac{\partial\epsilon_{kk}}{\partial\tau}d\tau. \tag{10}$$

4. Boundary conditions

The normal contact boundary conditions express the absence of overclosure between the outer boundaries of the two contacting entities, in a direction perpendicular to the rigid plane. Furthermore, across the actual contact surface, which is characterized by a positive pressure field, the lower portion of the coated sphere follows the shape of the rigid plane on which it rests, i.e.

$$H - \mathbf{x}(r_o,\phi,\theta).\mathbf{e}_y \geq 0, \quad \text{if } \sigma_y(r_o,\phi,\theta) = 0, \tag{11a}$$

$$H - \mathbf{x}(r_o,\phi,\theta).\mathbf{e}_y = 0, \quad \text{if } \sigma_y(r_o,\phi,\theta) < 0, \tag{11b}$$

where $\mathbf{e}_y$ is the unit vector pointing in the y-direction and σ_y corresponds to the normal traction field across the candidate contact surface.

The relative velocities w_{t_x} and w_{t_z} of the coated sphere with respect to the rigid plane, tangent to the contact interface in directions x and z, respectively, are given by

$$w_{t_x}(r_o,\phi,\theta) = V_s + \mathbf{v}(r_o,\phi,\theta).\mathbf{e}_x, \tag{12a}$$

$$w_{t_z}(r_o,\phi,\theta) = \mathbf{v}(r_o,\phi,\theta).\mathbf{e}_z. \tag{12b}$$

These differential speeds are equal to zero in regions of stick-contact where no slipping occurs. The tangential contact boundary conditions express Coulomb's law of surface friction (Coulomb, 1821)

$$\tau_{yx}(r_o,\phi,\theta)^2 + \tau_{yz}(r_o,\phi,\theta)^2 < \mu^2\sigma_y(r_o,\phi,\theta)^2, \quad \text{if } w_{t_x}^2 + w_{t_z}^2 = 0, \tag{13a}$$

$$\tau_{yx}(r_o,\phi,\theta)^2 + \tau_{yz}(r_o,\phi,\theta)^2 = \mu^2\sigma_y(r_o,\phi,\theta)^2, \quad \text{otherwise}, \tag{13b}$$

where τ_{ij} is the shear stress acting in the j-direction on a plane normal to the i-direction, and μ is Coulomb's friction coefficient.

5. Two-variable Fourier series

Due to the point symmetry of the coated sphere and to the fact that the rolling takes places in steady-state, and in a constant direction, any generic field $\hat{f}(r,\phi,\theta)$ in the continuum of the coating can be extended into a periodic function $f(r,\phi,\theta)$ of period 2π in both spatial variables ϕ, and θ (see Appendix A). A two variable Fourier series expansion of f writes

$$f(r,\phi,\theta) = \sum_{m,n=-\infty}^{\infty} f_{mn}(r)\, e^{im\phi} e^{in\theta}, \tag{14}$$

where the Fourier coefficients $f_{mn}(r)$ are given by

$$f_{mn}(r) = \frac{1}{(2\pi)^2} \int_{-\pi}^{\pi} e^{-im\phi} \left(\int_{0}^{\pi} f(r,\phi,\theta)\, e^{-in\theta} d\theta \right) d\phi. \tag{15}$$

Equations (14) and (15) are applied to the stresses, displacements and strains in the viscoelastic coating.

6. Geometric approximation

We wish to follow a typical procedure (e.g. Qiu, 2006, 2009; Zéhil and Gavin, 2013c,d) in transforming the sets of governing equations (8), (9) and (10) to the domain of Fourier coefficients by: (i) plugging expression (14) for the stresses, displacements and strains in the equations being transformed, (ii) multiplying by $\exp(-i(p\phi + q\theta))$ where p and q are integers, and (iii) integrating over one period (i.e. 2π) in the spatial variables ϕ and θ, to take advantage of the orthogonality property of complex exponentials. However, the dependence of certain coefficients in (8) and (9) on the spatial variable θ complicates this task significantly. This is shown in further detail in Appendix B.

To move forward with the proposed approach, it is convenient to assume, as is often the case in practice (see section 1), that the characteristic dimension of the contact surface is small compared to that of the rolling sphere, i.e. $r_c/R \ll 1$, or equivalently $d/R \ll 1$. Under this condition, the angular coordinate θ can be approximated by $\pi/2$ across the contact surface, which simplifies the sets of equations (8) and (9) significantly, so as to eliminate the coupling between Fourier coefficients of different orders. The equilibrium equations in (8) reduce to

$$\sigma_{rr,r} + \frac{1}{r}\sigma_{r\theta,\theta} + \frac{1}{r}\sigma_{r\phi,\phi} + \frac{1}{r}\left(2\sigma_{rr} - \sigma_{\theta\theta} - \sigma_{\phi\phi}\right) = \rho\Omega^2 \left(u_{r,\phi\phi} - 2u_{\phi,\phi} - (r + u_r)\right), \tag{16a}$$

$$\sigma_{r\phi,r} + \frac{1}{r}\sigma_{\theta\phi,\theta} + \frac{1}{r}\sigma_{\phi\phi,\phi} + \frac{3}{r}\sigma_{r\phi} = \rho\Omega^2 \left(u_{\phi,\phi\phi} - u_\phi + 2u_{r,\phi}\right), \tag{16b}$$

$$\sigma_{r\theta,r} + \frac{1}{r}\sigma_{\theta\theta,\theta} + \frac{1}{r}\sigma_{\theta\phi,\phi} + \frac{3}{r}\sigma_{r\theta} = \rho\Omega^2 u_{\theta,\phi\phi}, \tag{16c}$$

and the strain equations in (9) simplify to

$$\epsilon_{rr} = u_{r,r}, \tag{17a}$$

$$\epsilon_{\phi\phi} = \frac{1}{r}\left(u_{\phi,\phi} + u_r\right), \tag{17b}$$

$$\epsilon_{\theta\theta} = \frac{1}{r}\left(u_{\theta,\theta} + u_r\right), \tag{17c}$$

$$\epsilon_{r\phi} = \frac{1}{2}\left(\frac{1}{r}u_{r,\phi} + u_{\phi,r} - \frac{1}{r}u_\phi\right), \tag{17d}$$

$$\epsilon_{r\theta} = \frac{1}{2}\left(\frac{1}{r}u_{r,\theta} + u_{\theta,r} - \frac{1}{r}u_\theta\right), \tag{17e}$$

$$\epsilon_{\phi\theta} = \frac{1}{2r}\left(u_{\theta,\phi} + u_{\phi,\theta}\right). \tag{17f}$$

7. General solution to Fourier coefficients

Both sets of equations (16) and (17) can be expressed in terms of Fourier coefficients by substituting relevant fields by their Fourier series expansions (i.e equation (14)) and using the orthogonality property of complex exponentials. In the domain of Fourier coefficients, the equilibrium equations write

$$\dot{\sigma}_{rr_{mn}} + \frac{2}{r}\sigma_{rr_{mn}} - \frac{1}{r}\sigma_{\phi\phi_{mn}} - \frac{1}{r}\sigma_{\theta\theta_{mn}} + \frac{im}{r}\sigma_{r\phi_{mn}} + \frac{in}{r}\sigma_{r\theta_{mn}} + \rho\Omega^2\left(\left(1+m^2\right)u_{r_{mn}} + 2imu_{\phi_{mn}} + r\right) = 0, \tag{18a}$$

$$\dot{\sigma}_{r\phi_{mn}} + \frac{im}{r}\sigma_{\phi\phi_{mn}} + \frac{in}{r}\sigma_{\theta\phi_{mn}} + \frac{3}{r}\sigma_{r\phi_{mn}} + \rho\Omega^2\left(\left(1+m^2\right)u_{\phi_{mn}} - 2imu_{r_{mn}}\right) = 0, \tag{18b}$$

$$\dot{\sigma}_{r\theta_{mn}} + \frac{in}{r}\sigma_{\theta\theta_{mn}} + \frac{im}{r}\sigma_{\theta\phi_{mn}} + \frac{3}{r}\sigma_{r\theta_{mn}} + \rho\Omega^2 m^2 u_{\theta_{mn}} = 0, \tag{18c}$$

where the upper dot ($\dot{}$) denotes differentiation with respect to the spatial variable r. The strain equations in (17) are transformed into the Fourier domain, similarly, which yields

$$\epsilon_{rr_{mn}} = \dot{u}_{r_{mn}}, \tag{19a}$$

$$\epsilon_{\phi\phi_{mn}} = \frac{1}{r}\left(imu_{\phi_{mn}} + u_{r_{mn}}\right), \tag{19b}$$

$$\epsilon_{\theta\theta_{mn}} = \frac{1}{r}\left(inu_{\theta_{mn}} + u_{r_{mn}}\right), \tag{19c}$$

$$\epsilon_{r\phi_{mn}} = \frac{1}{2}\left(\frac{1}{r}imu_{r_{mn}} + \dot{u}_{\phi_{mn}} - \frac{1}{r}u_{\phi_{mn}}\right), \tag{19d}$$

$$\epsilon_{r\theta_{mn}} = \frac{1}{2}\left(\frac{1}{r}inu_{r_{mn}} + \dot{u}_{\theta_{mn}} - \frac{1}{r}u_{\theta_{mn}}\right), \tag{19e}$$

$$\epsilon_{\phi\theta_{mn}} = \frac{1}{2r}\left(imu_{\theta_{mn}} + inu_{\phi_{mn}}\right). \tag{19f}$$

The constitutive equations given by expression (10) are shifted into the 'frequency domain' as discussed in Appendix C, which yields

$$\sigma_{ij_{mn}}(r) = 2\mu_m^*\epsilon_{ij_{mn}}(r) + \lambda_m^*\epsilon_{kk_{mn}}(r)\,\delta_{ij}, \tag{20}$$

where $\omega_m = m\Omega$, $\mu_m^* = \mu^*(\omega_m) = i\omega_m\hat{\mu}(\omega_m)$, $\lambda_m^* = \lambda^*(\omega_m) = i\omega_m\hat{\lambda}(\omega_m)$, $\hat{\mu}(\omega_m)$ and $\hat{\lambda}(\omega_m)$ being the Fourier transforms of $\mu(t)$ and $\lambda(t)$, respectively.

After all governing equations have been transformed into the domain of Fourier coefficients, a set of six state variables is retained. These variables are arranged in a state vector $\mathbf{q}_{mn}$ as indicated below

$$\mathbf{q}_{mn}(r) = \langle \mathbf{d}_{mn}(r), \mathbf{f}_{mn}(r)\rangle^T, \tag{21}$$

where

$$\mathbf{d}_{mn}(r) = \left\langle u_{r_{mn}}(r), u_{\phi_{mn}}(r), u_{\theta_{mn}}(r)\right\rangle^T, \quad \text{and} \quad \mathbf{f}_{mn}(r) = \left\langle \sigma_{rr_{mn}}(r), \sigma_{r\phi_{mn}}(r), \sigma_{r\theta_{mn}}(r)\right\rangle^T. \tag{22}$$

Combining equations (18), (19) and (20), and eliminating non-state quantities yields the following system of ordinary differential equations in the state variables

$$\dot{u}_{r_{mn}} = -\mathcal{S}_{2_{mn}}^*(r)\left(2u_{r_{mn}} + imu_{\phi_{mn}} + inu_{\theta_{mn}}\right) + \mathcal{S}_{1_{mn}}^*\sigma_{rr_{mn}}, \tag{23a}$$

$$\dot{u}_{\phi_{mn}} = -\frac{im}{r}u_{r_{mn}} + \frac{1}{r}u_{\phi_{mn}} + \frac{1}{\mu_m^*}\sigma_{r\phi_{mn}}, \tag{23b}$$

$$\dot{u}_{\theta_{mn}} = -\frac{in}{r}u_{r_{mn}} + \frac{1}{r}u_{\theta_{mn}} + \frac{1}{\mu_m^*}\sigma_{r\theta_{mn}}, \tag{23c}$$

$$\dot{\sigma}_{rr_{mn}} = \mathcal{S}_{6_{mn}}(r)u_{r_{mn}} + \mathcal{S}_{7_{mn}}^*(r)u_{\phi_{mn}} + 2in\mathcal{S}_{4_{mn}}^*(r)u_{\theta_{mn}} - 4\mathcal{S}_{3_{mn}}^*(r)\sigma_{rr_{mn}} - \frac{im}{r}\sigma_{r\phi_{mn}} - \frac{in}{r}\sigma_{r\theta_{mn}} - \rho\Omega^2 r\delta_{m0}\delta_{n0}, \tag{23d}$$

$$\dot{\sigma}_{r\phi_{mn}} = -\mathcal{S}_{7_{mn}}^*(r)u_{r_{mn}} + \mathcal{S}_{8_{mn}}^*(r)u_{\phi_{mn}} + mn\mathcal{S}_{4_{mn}}^*(r)u_{\theta_{mn}} - im\mathcal{S}_{2_{mn}}^*(r)\sigma_{rr_{mn}} - \frac{3}{r}\sigma_{r\phi_{mn}}, \tag{23e}$$

$$\dot{\sigma}_{r\theta_{mn}} = -2in\mathcal{S}^*_{4_{mn}}(r)u_{r_{mn}} + mn\mathcal{S}^*_{4_{mn}}(r)u_{\phi_{mn}} + \mathcal{S}^*_{9_{mn}}(r)u_{\theta_{mn}} - in\mathcal{S}^*_{2_{mn}}(r)\sigma_{rr_{mn}} - \frac{3}{r}\sigma_{r\theta_{mn}}, \tag{23f}$$

where $S^*_{1_{mn}}, S^*_{2_{mn}}, \ldots, S^*_{9_{mn}}$ are shorthand parameters defined below

$$\mathcal{S}^*_{1_{mn}} = 1/\left(\lambda^*_m + 2\mu^*_m\right), \tag{24a}$$
$$\mathcal{S}^*_{2_{mn}}(r) = \lambda^*_m \mathcal{S}^*_{1_m}/r, \tag{24b}$$
$$\mathcal{S}^*_{3_{mn}}(r) = \mu^*_m \mathcal{S}^*_{1_m}/r, \tag{24c}$$
$$\mathcal{S}^*_{4_{mn}}(r) = \left(3\lambda^*_m + 2\mu^*_m\right)\mathcal{S}^*_{3_m}(r)/r, \tag{24d}$$
$$\mathcal{S}^*_{5_{mn}}(r) = \left(\lambda^*_m + \mu^*_m\right)\mathcal{S}^*_{3_m}(r)/r, \tag{24e}$$
$$\mathcal{S}^*_{6_{mn}}(r) = 4\mathcal{S}^*_{4_m}(r) - \rho\Omega^2\left(1 + m^2\right), \tag{24f}$$
$$\mathcal{S}^*_{7_{mn}}(r) = 2im\left(\mathcal{S}^*_{4_m}(r) - \rho\Omega^2\right), \tag{24g}$$
$$\mathcal{S}^*_{8_{mn}}(r) = 4m^2\mathcal{S}^*_{5_m}(r) + n^2\mu^*_m/r^2 - \rho\Omega^2\left(1 + m^2\right), \tag{24h}$$
$$\mathcal{S}^*_{9_{mn}}(r) = 4n^2\mathcal{S}^*_{5_m}(r) + m^2\mu^*_m/r^2 - \rho\Omega^2 m^2. \tag{24i}$$

By analogy to forced time-varying systems in linear system theory (e.g. Lygeros and Ramponi, 2010), equations (23) can be written in the form

$$\dot{\mathbf{q}}_{mn}(r) = \mathbf{A}_{mn}(r)\,\mathbf{q}_{mn}(r) + \mathbf{b}_{mn}(r) \tag{25}$$

where the 6×6 complex-valued matrix $\mathbf{A}_{mn}(r)$ is given by

$$\mathbf{A}_{mn}(r) = \begin{bmatrix} -2\mathcal{S}^*_{2_{mn}}(r) & -im\mathcal{S}^*_{2_{mn}}(r) & -in\mathcal{S}^*_{2_{mn}}(r) & \mathcal{S}^*_{1_{mn}} & 0 & 0 \\ -im/r & 1/r & 0 & 0 & 1/\mu^*_m & 0 \\ -in/r & 0 & 1/r & 0 & 0 & 1/\mu^*_m \\ \mathcal{S}^*_{6_{mn}}(r) & \mathcal{S}^*_{7_{mn}}(r) & 2in\mathcal{S}^*_{4_{mn}}(r) & -4\mathcal{S}^*_{3_{mn}}(r) & -im/r & -in/r \\ -\mathcal{S}^*_{7_{mn}}(r) & \mathcal{S}^*_{8_{mn}}(r) & mn\mathcal{S}^*_{4_{mn}}(r) & -im\mathcal{S}^*_{2_{mn}}(r) & -3/r & 0 \\ -2in\mathcal{S}^*_{4_{mn}}(r) & mn\mathcal{S}^*_{4_{mn}}(r) & \mathcal{S}^*_{9_{mn}}(r) & -in\mathcal{S}^*_{2_{mn}}(r) & 0 & -3/r \end{bmatrix}, \tag{26}$$

and the 'forcing' term $\mathbf{b}_{mn}(r)$, resulting from the Coriolis effect, writes

$$\mathbf{b}_{mn}(r) = \left\langle 0, 0, 0, -\rho\Omega^2 r\delta_{m0}\delta_{n0}, 0, 0\right\rangle^T. \tag{27}$$

The solution to system (25) is of the form

$$\mathbf{q}_{mn}(r) = \mathbf{T}_{mn}(r, r_i)\,\mathbf{q}_{mn}(r_i) + \mathbf{J}_{mn}(r, r_i), \tag{28}$$

where $\mathbf{J}_{mn}(r, r_i)$ is given by

$$\mathbf{J}_{mn}(r, r_i) = \int_{r_i}^{r} \mathbf{T}_{mn}(r, s)\,\mathbf{b}_{mn}(s)\,ds, \tag{29}$$

and $\mathbf{T}_{mn}(r, r_i)$ corresponds to the state-transition matrix. Equation 28 can be written in the form

$$\begin{bmatrix} \mathbf{d}_{mn}(r) \\ \mathbf{f}_{mn}(r) \end{bmatrix} = \begin{bmatrix} \mathbf{T}_{mn,11}(r, r_i) & \mathbf{T}_{mn,12}(r, r_i) \\ \mathbf{T}_{mn,21}(r, r_i) & \mathbf{T}_{mn,22}(r, r_i) \end{bmatrix} \times \begin{bmatrix} \mathbf{d}_{mn}(r_i) \\ \mathbf{f}_{mn}(r_i) \end{bmatrix} + \begin{bmatrix} \mathbf{J}_{mn}(r, r_i)(1:3) \\ \mathbf{J}_{mn}(r, r_i)(4:6) \end{bmatrix}, \tag{30}$$

where $\mathbf{J}_{mn}(r, r_i)(p:q)$ denotes the subvector of $\mathbf{J}_{mn}(r, r_i)$ comprising its components p through q. Incorporating the boundary conditions at $r = r_i$, i.e. $\mathbf{d}_{mn}(r_i) = \mathbf{0}$, Fourier coefficients of displacements and stresses at r are related explicitly

$$\mathbf{d}_{mn}(r) = \mathbf{T}_{mn,12}(r, r_i)\mathbf{T}^{-1}_{mn,22}(r, r_i)\left(\mathbf{f}_{mn}(r) - \mathbf{J}_{mn}(r, r_i)(4:6)\right) + \mathbf{J}_{mn}(r, r_i)(1:3). \tag{31}$$

The evaluation of $\mathbf{T}_{mn}(r, r_i)$ can be carried out numerically, to the desired degree of accuracy, using the block-pulse technique proposed by Rammohan Rao and Ganapathy (1979). As a more efficient and straightforward alternative,

the integration domain $[r_i, r]$ is divided into n_r sub-intervals of equal size $\Delta r = (r_o - r)/n_r$, and the state-transition matrix $\mathbf{T}_{mn}(r, r_i)$ is written as

$$\mathbf{T}_{mn}(r, r_i) = \prod_{k=1}^{n_r} \mathbf{e}^{\Delta r \mathbf{A}_k}, \tag{32}$$

where $\mathbf{A}_k = \mathbf{A}_{mn}(r_i + (k - \alpha)\Delta r)$, with α chosen in $[0, 1]$. Evaluating expression (29) requires numerical integration, which is computationally expensive. Fortunately, in the present case, a single evaluation is necessary since $\mathbf{b}_{mn} \neq \mathbf{0}$, and hence $\mathbf{J}_{mn}(r, r_i) \neq \mathbf{0}$, for $m = n = 0$, only.

8. Case of multiple layers

Solution (28) is readily adapted to the case of a hard sphere coated with multiple (k) layers of different thickness and material characteristics. Contacting layers are bonded to one another, the first being attached to the hard core. This case is illustrated in figure 2. Using an upper index to denote layer numbering, the continuity of displacements and stresses across the interface between layers $j - 1$ and j writes

$$\mathbf{q}_{mn}^{(j-1)}(r_{(j-1)j}) = \mathbf{q}_{mn}^{(j)}(r_{(j-1)j}). \tag{33}$$

By combining equations (28) and (33) for layers 1 through k, it can be shown that $\mathbf{q}_{mn}^{k}(r_o)$ is given by

$$\mathbf{q}_{mn}^{k}(r_o) = \left(\prod_{j=1}^{k} \mathbf{T}_{mn}^{(j)} \right) \mathbf{q}_{mn}^{1}(r_i) + \sum_{j=1}^{k-1} \left(\prod_{i=j+1}^{k} \mathbf{T}_{mn}^{(i)} \right) \mathbf{J}_{mn}^{j}\left(r_{j(j+1)}\right) + \mathbf{J}_{mn}^{k}(r_o) \tag{34}$$

where $\mathbf{T}_{mn}^{(j)} = \mathbf{T}_{mn}^{(j)}\left(r_{j(j+1)}, r_{(j-1)j}\right)$.

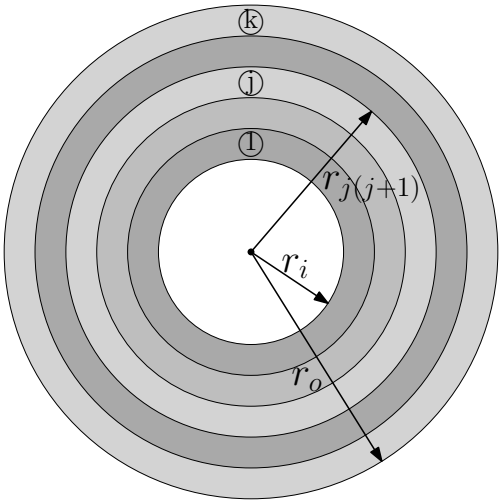

Figure 2: Rigid sphere coated with multiple viscoelastic layers.

9. Boundary element formulation

The candidate contact surface on the outer boundary of the viscoelastic coating is discretized into $N_T = K_\phi K_\theta$ nodes, as illustrated in figures 3(a) and 3(b), with angular spacings between nodes $\Delta\phi$ and $\Delta\theta$. A global number $A = i + (j - 1)K_\phi$ is assigned to each node.

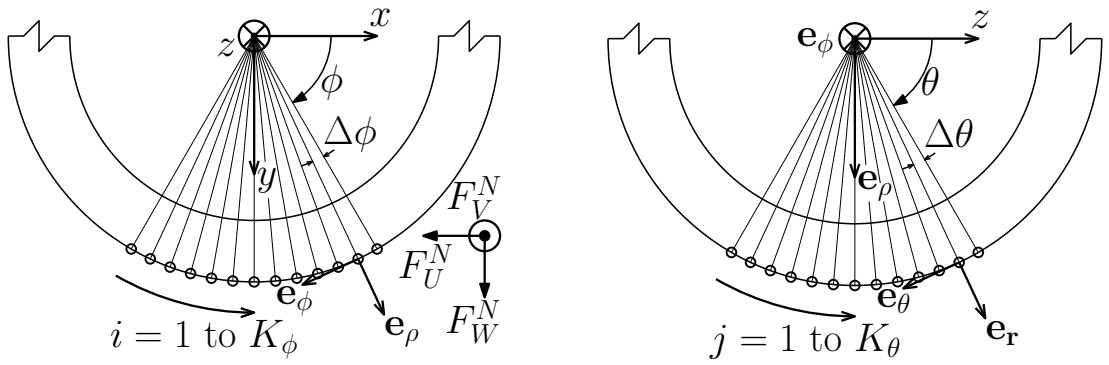

(a) nodal grid in ϕ (b) nodal grid in θ

Figure 3: Discretization of the candidate contact surface.

The nodal displacement vector $\mathbf{D}_s = \left\langle \mathbf{D}_R^T, \mathbf{D}_\Phi^T, \mathbf{D}_\Theta^T \right\rangle^T$ is related to the nodal force vector $\mathbf{F}_s = \left\langle \mathbf{F_R}^T, \mathbf{F_\Phi}^T, \mathbf{F_\Theta}^T \right\rangle^T$ through a boundary-element compliance matrix $\mathbf{C}_s$ according to

$$\begin{bmatrix} \mathbf{C}_{RR} & \mathbf{C}_{R\Phi} & \mathbf{C}_{R\Theta} \\ \mathbf{C}_{\Phi R} & \mathbf{C}_{\Phi\Phi} & \mathbf{C}_{\Phi\Theta} \\ \mathbf{C}_{\Theta R} & \mathbf{C}_{\Theta\Phi} & \mathbf{C}_{\Theta\Theta} \end{bmatrix} \begin{bmatrix} \mathbf{F}_R \\ \mathbf{F}_\Phi \\ \mathbf{F}_\Theta \end{bmatrix} + d_R^{(c)} \begin{bmatrix} \mathbf{1} \\ \mathbf{0} \\ \mathbf{0} \end{bmatrix} = \begin{bmatrix} \mathbf{D}_R \\ \mathbf{D}_\Phi \\ \mathbf{D}_\Theta \end{bmatrix}, \tag{35}$$

where the subscript "s" refers to the system of spherical coordinates attached to point C, indices R, Φ and Θ refer to the spatial coordinates of the same name, and $d_R^{(c)}$ is the (uniform) radial displacement due to the Coriolis effect, i.e. retaining the first row of (31), with $m = n = 0$

$$d_R^{(c)} = \mathbf{J}_{00}(r, r_i)(1) - \mathbf{T}_{00,12}(r, r_i)(1, :)\mathbf{T}_{00,22}^{-1}(r, r_i)\mathbf{J}_{00}(r, r_i)(4 : 6). \tag{36}$$

10. Building the compliance matrix

Each entry $C_{PQ}(M, N)$ of matrix $\mathbf{C}_s$ corresponds to the displacement of node M in direction $P \in \{R, \Phi, \Theta\}$ under the influence of a unit point load F_Q^N applied at node N, in direction $Q \in \{R, \Phi, \Theta\}$. Based on this interpretation, matrix $\mathbf{C}_s$ is formed in three conceptual steps:

(i) a 2π-periodic rectangular distribution of surface stresses $\sigma_Q^N(r_o, \phi, \theta)$ is associated with F_Q^N

$$\sigma_Q^N(r_o, \phi, \theta) = \begin{cases} \frac{F_Q^N}{r_o^2 \sin(\theta)\Delta\phi\Delta\theta}, & \text{if} \begin{cases} \phi^N - \frac{\Delta\phi}{2} \le \phi \le \phi^N + \frac{\Delta\phi}{2} \\ \theta^N - \frac{\Delta\theta}{2} \le \theta \le \theta^N + \frac{\Delta\theta}{2} \end{cases} \\ 0, & \text{otherwise.} \end{cases}, \tag{37}$$

(ii) the Fourier series coefficients of the surface stress field given by (37) are computed from their analytical expression below, where $\mathrm{sinc}(\zeta) = \sin(\zeta)/\zeta$:

$$\sigma_{Q_{mn}}^N(r) = \frac{F_Q^N}{(2\pi r_o)^2} \mathrm{sinc}\left(m\frac{\Delta\phi}{2}\right) e^{-im\phi^N} \frac{1}{\Delta\theta} \int_{\theta^N - \frac{\Delta\theta}{2}}^{\theta^N + \frac{\Delta\theta}{2}} \frac{1}{\sin(\theta)} e^{-in\theta^N} d\theta, \tag{38}$$

(iii) the Fourier series coefficients of the displacements at point M are deduced from (38) using equation (31).

11. Solving the rolling contact problem

Because the contact interface is flat and lies in the rigid plane supporting the rolling sphere, the solution to the rolling contact problem is better addressed in a rectangular system of coordinates. To this end, alternative nodal force and displacement vectors are defined by

$$\mathbf{F}_s^N = \mathbf{Q}^N \mathbf{F}_r^N \quad \text{and} \quad \mathbf{D}_s^N = \mathbf{Q}^N \mathbf{D}_r^N, \tag{39}$$

where the subscripts "r" and "s" refer to rectangular and spherical coordinates, respectively, the superscript "N" corresponds to the node number, $\mathbf{F}_s^N = \left\langle F_R^N, F_\Phi^N, F_\Theta^N \right\rangle^T$, $\mathbf{D}_s^N = \left\langle D_R^N, D_\Phi^N, D_\Theta^N \right\rangle^T$, $\mathbf{F}_r^N = \left\langle F_W^N, F_U^N, F_V^N \right\rangle^T$, $\mathbf{D}_r^N = \left\langle D_W^N, D_U^N, D_V^N \right\rangle^T$, and the nodal transformation matrix $\mathbf{Q}^N$ is given by

$$\mathbf{Q}^N = \begin{bmatrix} \sin(\theta^N) sin(\phi^N) & -\sin(\theta^N) cos(\phi^N) & -cos(\theta^N) \\ \cos(\phi^N) & sin(\phi^N) & 0 \\ \cos(\theta^N) sin(\phi^N) & -\cos(\theta^N) cos(\phi^N) & \sin(\theta^N) \end{bmatrix}. \tag{40}$$

The nodal force components F_W^N, F_U^N and F_V^N in the rectangular system of coordinates are counted positively when acting on the external boundary of the sphere's coating as shown in figure 3(a). The nodal expressions in (39) can be assembled into global transformation equations, i.e.

$$\mathbf{F}_s = \mathbf{Q}\mathbf{F}_r \quad \text{and} \quad \mathbf{D}_s = \mathbf{Q}\mathbf{D}_r, \tag{41}$$

where $\mathbf{Q}$ is a $3N_T \times 3N_T$ unitary global transformation matrix. Matrix $\mathbf{Q}$ comprises nine $N_T \times N_T$ purely diagonal blocs, i.e.

$$\mathbf{Q} = \begin{bmatrix} \mathbf{Q}_{RW} & \mathbf{Q}_{RU} & \mathbf{Q}_{RV} \\ \mathbf{Q}_{\Phi W} & \mathbf{Q}_{\Phi U} & \mathbf{0} \\ \mathbf{Q}_{\Theta W} & \mathbf{Q}_{\Theta U} & \mathbf{Q}_{\Theta V} \end{bmatrix}. \tag{42}$$

The diagonals of the blocs shown in (42) are given by

$$\operatorname{diag}(\mathbf{Q}_{RW}) = \left\langle +\sin(\theta^1)\sin(\phi^1), \ \ldots \ , +\sin(\theta^{N_T})\sin(\phi^{N_T}) \right\rangle, \tag{43a}$$

$$\operatorname{diag}(\mathbf{Q}_{RU}) = \left\langle -\sin(\theta^1)\cos(\phi^1), \ \ldots \ , -\sin(\theta^{N_T})\cos(\phi^{N_T}) \right\rangle, \tag{43b}$$

$$\operatorname{diag}(\mathbf{Q}_{RV}) = \left\langle -\cos(\theta^1), \ \ldots \ , -\cos(\theta^{N_T}) \right\rangle, \tag{43c}$$

$$\operatorname{diag}(\mathbf{Q}_{\Phi W}) = \left\langle +\cos(\phi^1), \ \ldots \ , +\cos(\phi^{N_T}) \right\rangle, \tag{43d}$$

$$\operatorname{diag}(\mathbf{Q}_{\Phi U}) = \left\langle +\sin(\phi^1), \ \ldots \ , +\sin(\phi^{N_T}) \right\rangle, \tag{43e}$$

$$\operatorname{diag}(\mathbf{Q}_{\Theta W}) = \left\langle +\cos(\theta^1)\sin(\phi^1), \ \ldots \ , +\cos(\theta^{N_T})\sin(\phi^{N_T}) \right\rangle, \tag{43f}$$

$$\operatorname{diag}(\mathbf{Q}_{\Theta U}) = \left\langle -\cos(\theta^1)\cos(\phi^1), \ \ldots \ , -\cos(\theta^{N_T})\cos(\phi^{N_T}) \right\rangle, \tag{43g}$$

$$\operatorname{diag}(\mathbf{Q}_{\Theta V}) = \left\langle +\sin(\theta^1), \ \ldots \ , +\sin(\theta^{N_T}) \right\rangle. \tag{43h}$$

The boundary element formulation of the viscoelastic coating is expressed in rectangular coordinates by combining equations (35) and (41), which yields

$$\mathbf{C}_r \mathbf{F}_r + \mathbf{D}_r^{(c)} = \mathbf{D}_r, \tag{44}$$

where $\mathbf{C}_r = \mathbf{Q}^T \mathbf{C}_s \mathbf{Q}$ is the compliance matrix and $\mathbf{D}_r^{(c)} = \langle \operatorname{diag}(\mathbf{Q}_{RW}), \operatorname{diag}(\mathbf{Q}_{RU}), \operatorname{diag}(\mathbf{Q}_{RV}) \rangle^T$ is the vector of nodal displacements due to the Coriolis effect, in rectangular coordinates. It is helpful to write equation (44) in more explicit form as

$$\begin{bmatrix} \mathbf{C}_{WW} & \mathbf{C}_{WU} & \mathbf{C}_{WV} \\ \mathbf{C}_{UW} & \mathbf{C}_{UU} & \mathbf{C}_{UV} \\ \mathbf{C}_{VW} & \mathbf{C}_{VU} & \mathbf{C}_{VV} \end{bmatrix} \begin{bmatrix} \mathbf{F}_W \\ \mathbf{F}_U \\ \mathbf{F}_V \end{bmatrix} + d_R^{(c)} \begin{bmatrix} \operatorname{diag}(\mathbf{Q}_{RW}) \\ \operatorname{diag}(\mathbf{Q}_{RU}) \\ \operatorname{diag}(\mathbf{Q}_{RV}) \end{bmatrix} = \begin{bmatrix} \mathbf{D}_W \\ \mathbf{D}_U \\ \mathbf{D}_V \end{bmatrix}. \tag{45}$$

The rolling contact problem may be solved, for instance, by extending the contact algorithms proposed by Zéhil and Gavin (2013a) to the case of a deformable object rolling on a rigid plane. Equation (45) reduces, for the vertical behavior, to

$$\mathbf{C}_{WW}\mathbf{F}_W + \mathbf{C}_{WU}\mathbf{F}_U + \mathbf{C}_{WV}\mathbf{F}_V + d_R^{(c)}\,\mathrm{diag}\,(\mathbf{Q}_{RW}) = \mathbf{D}_W. \tag{46}$$

In the following, a scalar function applied to an array (arrays are typed in bold) operates on each of the array's elements. Likewise, the product of two arrays of the same size is meant as an element-by-element multiplication. Also, the addition of a scalar to an array corresponds to adding the scalar to each element of the array. The characters "c" and "$\bar{c}$", used as arguments of a given array, stand for extracting from this array the rows/columns corresponding to contact nodes and free nodes respectively. Alternatively, the argument ":" stands for "all" rows or columns. Finally, the symbol $\mathbf{1}$ designates a column vector whose size follows naturally from the context, and whose components are all equal to unity.

It is here assumed, as will be substantiated below, that the horizontal nodal force fields $\mathbf{F}_U$ and $\mathbf{F}_V$ are given. The vertical nodal forces at the free nodes are also known, i.e. $\mathbf{F}_W(\bar{c}) = \mathbf{0}$. The restriction of system (46) to the contact nodes must therefore be solved for the unknown contact forces $\mathbf{F}_W(c)$, i.e.

$$\mathbf{C}_{WW}(c,c)\mathbf{F}_W(c) + \mathbf{C}_{WU}(c,:)\mathbf{F}_U + \mathbf{C}_{WV}(c,:)\mathbf{F}_V + d_R^{(c)}\,\mathrm{diag}\,(\mathbf{Q}_{RW})\,(c) = \mathbf{D}_W(c). \tag{47}$$

To this end, vertical nodal displacements across the contact surface $\mathbf{D}_W(c)$ may be expressed, according to the normal boundary condition (11b), in terms of the additional unknown H (see figure 1) as

$$\mathbf{D}_W(c) \approx H - r_o \sin\left(\boldsymbol{\theta}(c)\right) \sin\left(\boldsymbol{\phi}(c)\right), \tag{48}$$

which requires one additional equation provided by the vertical equilibrium of the sphere, i.e.

$$\mathbf{1}^T\mathbf{F}_W(c) + P = 0. \tag{49}$$

Equations (47) and (49) are then combined into an augmented system in the unknowns $\mathbf{F}_W(c)$ and H

$$\begin{bmatrix} \mathbf{C}_{WW}(c,c) & -\mathbf{1} \\ \mathbf{1}^T & 0 \end{bmatrix} \begin{bmatrix} \mathbf{F}_W(c) \\ H \end{bmatrix} = -\begin{bmatrix} \mathbf{q} \\ P \end{bmatrix}, \tag{50}$$

where the shorthand vector $\mathbf{q}$ is given by

$$\mathbf{q} = r_o \sin\left(\boldsymbol{\theta}(c)\right) \sin\left(\boldsymbol{\phi}(c)\right) + d_R^{(c)}\,\mathrm{diag}\,(\mathbf{Q}_{RW})\,(c) + \mathbf{C}_{WU}(c,:)\mathbf{F}_U + \mathbf{C}_{WV}(c,:)\mathbf{F}_V. \tag{51}$$

It is convenient to assume, as later justified in sections 13 and 14.3, that surface friction is negligible, in which case $\mathbf{F}_U = \mathbf{F}_V = \mathbf{0}$. Under these conditions, a "normal-contact" algorithm is readily set up, as descried by Zéhil and Gavin (2013a), to solve system (50) while iterating on the subset of contact nodes to satisfy the normal boundary conditions (11), i.e. to achieve negative tractions across the contact area and eliminate the overclosures characterized by the inequality

$$\mathbf{D}_W(c) + r_o \sin\left(\boldsymbol{\theta}(c)\right) \sin\left(\boldsymbol{\phi}(c)\right) - H \geq 0. \tag{52}$$

12. Aspects of computational efficiency

In this section, we briefly discuss a few aspects of computational efficiency in the implementation of the proposed modeling and solving strategies:

- According to the transformation equation $\mathbf{C}_r = \mathbf{Q}^T\mathbf{C}_s\mathbf{Q}$, forming $\mathbf{C}_{WW}$, which, in the absence of surface friction, is the only part of $\mathbf{C}_r$ needed for the solution of the rolling contact problem (50), requires building the full compliance matrix $\mathbf{C}_s$ in spherical coordinates, as well as the full transformation matrix $\mathbf{Q}$. A cheaper alternative, from a computational aspect, would be to take advantage of the fact that, under small strains, the reference configuration and the deformed configuration are very close to each other, which renders the constitutive equations formulated in one configuration applicable in the other, i.e. practically $\mathbf{C}_{WW} \approx \mathbf{C}_{RR}$. Both approaches were implemented by the authors and yielded comparable results: for instance, with the parameters retained in section 14, relative differences in the resisting torque of less than 3% were observed, up to 12% strains.

- In building parts of the compliance matrix $\mathbf{C}_s$ of a spherical viscoelastic layer rolling about the horizontal z-axis, advantage can be taken from configurational similarities and symmetry, but to a lesser extent than in the case discussed by Zéhil and Gavin (2013c,b) of a plane layer punched by a moving indenter. In the present case (see figure 3), due to symmetry in the transverse direction, only nodes located in, and on one side of, the xy-plane need be considered. Furthermore, two pairs of nodes located on the same nodal rows (constant j and θ) and in the same relative position with respect to each other in the ϕ-coordinate will behave in the same way. Consequently, unit point loads need be applied at only the first ($i = 1$) and last ($i = K_\phi$) node of a nodal row. By implementing these changes, the computational cost of building a full compliance matrix is reduced from the order of N_T^2 to the order of $N_T^{3/2}$.

- To avoid numerical integration in computing the Fourier series coefficients of the surface stress field from their general expression in (38), the term $\sin(\theta)$ in the integrand may be approximated by 1 across the candidate contact surface, in which case equation (38) simplifies to

$$\sigma^N_{Q_{mn}}(r) \approx \frac{F^N_Q}{(2\pi r_o)^2} \operatorname{sinc}\left(m\frac{\Delta\phi}{2}\right) \operatorname{sinc}\left(n\frac{\Delta\theta}{2}\right) e^{-i\left(m\phi^N + n\theta^N\right)}. \tag{53}$$

  The difference between expressions (38) and (53) was tested under the assumptions retained in this work, and it was found to be numerically small. For instance, with the parameters retained in section 14, the relative change in rolling resistance is well within 0.1%.

13. Considerations related to surface friction

It is interesting to note that, in the absence of surface friction, a deformable viscoelastic solid does not incur any resistance when sliding in steady-state, without rolling, on a rigid plane. This is due to the absence of any dynamics in the viscoelastic continuum, the deformation field being independent of time. Referring back to figure 1 for the coated sphere, it is also noteworthy that, in the absence of surface friction, the resultant of the (normal) contact stress field acts in the vertical direction, because the contact surface is flat, and horizontal. As a consequence, the horizontal driving force Q cannot be balanced. We hence gather that, without surface friction, the linear velocity V_s of point C as well as the driving force Q are undetermined, and therefore irrelevant. The frictionless problem is therefore restricted to the coated sphere spinning under the influence of the driving torque T, which is balanced by an equal and opposite resisting torque T_r generated by the horizontal offset of the normal contact force, $-P$.

In the presence of surface friction, two additional phenomena contribute to increasing, or decreasing, the resistance incurred by the rolling sphere:

1. the field of contact shear stresses influences the normal contact stress distribution, which modifies the offset of its vertical resultant. Analytical and numerical studies suggest that this influence is, in many cases, limited. It is expected to be increasingly so, inasmuch as (i) the coefficient of surface friction is small, (ii) the deformable material is less compressible, and (iii) the characteristic dimension of the contact surface is small as compared to the thickness of the coating (e.g. Bogy, 1968; Kuznetsov, 1978; Scheibert et al., 2009),
2. slipping occurs in regions of the contact surface where the contact shear stress reaches Coulomb's limit. Thus, further dissipation arises from the work of shear stresses in the slipping regions. However, because parts of the interface remain in a state of stick-contact, the differential velocities in the slipping regions are due to local deformation dynamics only, and are hence of limited magnitude. It follows that, in most cases of partial slipping, the contribution of slipping friction to rolling resistance will also be limited, as noted for instance by Greenwood and Tabor (1958); Qiu (2006); Tabor (1955); Zéhil and Gavin (2013c).

It is worth mentioning that, if generalized slipping occurs across the entire contact surface, as opposed to the case of partial slipping, the differential velocities are mostly governed by indeterminate global kinematics, i.e. Ω and V_s, which results in rolling resistance being arbitrarily large. However, this 'extreme' case is not of direct interest to us.

In the following, the characters "s" and "$\bar{s}$", used as arguments, stand for extracting from a given array the rows/columns corresponding to stick-contact nodes and slipping nodes, respectively. The solution to the frictional rolling contact problem, at a given angular speed Ω, involves determining, in addition to the nodal normal force vector

$\mathbf{F}_W(c)$ and the distance H, the nodal tangential force vectors $\mathbf{F}_U(s)$ and $\mathbf{F}_V(s)$ across the regions of stick-contact, and the unknown linear speed V_s. The solution process may conceptually be 'decoupled' into

(i) a "normal-contact" subroutine, similar to that described in section 11, solving for $\mathbf{F}_W(c)$ and H, given $\mathbf{F}_U$ and $\mathbf{F}_V$, as provided by the "stick-slip" subroutine (see below), and
(ii) a "stick-slip" subroutine, solving for $\mathbf{F}_U(s)$, $\mathbf{F}_V(s)$ and V_s, given $\mathbf{F}_W(c)$, as provided by the "normal-contact" subroutine.

These two algorithms are combined in an iterative solving scheme starting from $\mathbf{F}_U = \mathbf{F}_V = \mathbf{0}$, as an initial guess, and converging to the fully coupled solution of the rolling contact problem. The present section briefly outlines the structure of the "stick-slip" subroutine. The latter is based on the restriction of equations (45) to stick-contact nodes $N_{i,j}$, expressed as

$$\mathbf{C}_{UU}(N_{i,j},s)\mathbf{F}_U(s)+\mathbf{C}_{UV}(N_{i,j},s)\mathbf{F}_V(s)=\mathbf{D}_U(N_{i,j})-\mathbf{C}_{UW}(N_{i,j},c)\mathbf{F}_W(c)-\mathbf{C}_{UU}(N_{i,j},\bar{s})\mathbf{F}_U(\bar{s})-\mathbf{C}_{UV}(N_{i,j},\bar{s})\mathbf{F}_V(\bar{s})-d_R^{(c)}\,\mathrm{diag}\,(\mathbf{Q}_{RU})\left(N_{i,j}\right), \tag{54a}$$

$$\mathbf{C}_{VU}(N_{i,j},s)\mathbf{F}_U(s)+\mathbf{C}_{VV}(N_{i,j},s)\mathbf{F}_V(s)=\mathbf{D}_V(N_{i,j})-\mathbf{C}_{VW}(N_{i,j},c)\mathbf{F}_W(c)-\mathbf{C}_{VU}(N_{i,j},\bar{s})\mathbf{F}_U(\bar{s})-\mathbf{C}_{VV}(N_{i,j},\bar{s})\mathbf{F}_V(\bar{s})-d_R^{(c)}\,\mathrm{diag}\,(\mathbf{Q}_{RV})\left(N_{i,j}\right), \tag{54b}$$

where it is assumed that $\mathbf{F}_W(c)$ is known, and that $\mathbf{F}_U(\bar{s})$ and $\mathbf{F}_V(\bar{s})$ follow Coulomb's law of surface friction. Before system (54) can be solved for $\mathbf{F}_U(s)$ and $\mathbf{F}_V(s)$, expressions for the horizontal displacements $\mathbf{D}_U(N_{i,j})$ and $\mathbf{D}_V(N_{i,j})$, appearing on the right-hand-sides of equations (54a) and (54b), are determined from equations (12). The conditions $w_{t_x}=0$ and $w_{t_z}=0$ in regions of stick contact write

$$u_{x,\phi}=r_o\sin(\theta)\sin(\phi)-\frac{V_s}{\Omega}-\cos(\phi)^2\,u_y+\sin(\phi)\cos(\phi)\,u_x\approx r_o-\frac{V_s}{\Omega}, \tag{55a}$$

$$u_{z,\phi}=0. \tag{55b}$$

Using a finite difference approach, $\mathbf{D}_U(N_{i,j})$ and $\mathbf{D}_V(N_{i,j})$ are related, through equations (55), to $\mathbf{D}_U(N_{i_{ref}(j)+1,j})$ and $\mathbf{D}_V(N_{i_{ref}(j)+1,j})$, where the index "$i_{ref}(j)$" refers to the leading edge stick contact node on nodal row j

$$\mathbf{D}_U\left(N_{i,j}\right)=\mathbf{D}_U\left(N_{i_{ref}(j)+1,j}\right)+\left(\frac{V_s}{\Omega}-r_o\right)\left(i_{ref}(j)+1-i\right)\Delta\phi, \tag{56a}$$

$$\mathbf{D}_V\left(N_{i,j}\right)=\mathbf{D}_V\left(N_{i_{ref}(j)+1,j}\right). \tag{56b}$$

Because the $N_{i_{ref}(j)+1,j}$ correspond to slipping nodes, or to free nodes, the additional unknowns $\mathbf{D}_U\left(N_{i_{ref}(j)+1,j}\right)$ and $\mathbf{D}_V\left(N_{i_{ref}(j)+1,j}\right)$ can be associated with as many additional equations taken from system (45)

$$\mathbf{D}_U\left(N_{i_{ref}(j)+1,j}\right)=\mathbf{C}_{UW}(N_{i_{ref}(j)+1,j},c)\mathbf{F}_W(c)+\mathbf{C}_{\mathbf{UU}}((N_{i_{ref}(j)+1,j},c)\mathbf{F}_U(c)+\mathbf{C}_{UV}(N_{i_{ref}(j)+1,j},c)\mathbf{F}_V(c)+d_R^{(c)}\,\mathrm{diag}\,(\mathbf{Q}_{RU})\left(N_{i_{ref}(j)+1,j}\right), \tag{57a}$$

$$\mathbf{D}_V\left(N_{i_{ref}(j)+1,j}\right)=\mathbf{C}_{VW}(N_{i_{ref}(j)+1,j},c)\mathbf{F}_W(c)+\mathbf{C}_{VU}((N_{i_{ref}(j)+1,j},c)\mathbf{F}_U(c)+\mathbf{C}_{VV}(N_{i_{ref}(j)+1,j},c)\mathbf{F}_V(c)+d_R^{(c)}\,\mathrm{diag}\,(\mathbf{Q}_{RV})\left(N_{i_{ref}(j)+1,j}\right). \tag{57b}$$

The unknown velocity V_s appearing in expression (56a) requires one additional equation provided by balancing the torque about the z-axis

$$\mathbf{1}^T\mathbf{F}_U(s)+\mathbf{0}^T\mathbf{F}_V(s)+0.V_s=-\frac{T}{H}-\frac{r_o}{H}\left[\sin(\boldsymbol{\theta}(c))\cos(\boldsymbol{\theta}(c))\right]^T\mathbf{F}_W(c)-\mathbf{1}^T\mathbf{F}_U(\bar{s}). \tag{58}$$

Combining equations (54) to (58) leads to a system of equations in the unknowns $\mathbf{F}_U(s)$, $\mathbf{F}_V(s)$ and V_s

$$\begin{aligned}&\mathbf{G}_{UU}(N_{i,j},s)\mathbf{F}_U(s)+\mathbf{G}_{UV}(N_{i,j},s)\mathbf{F}_V(s)-\left(g_{ij}/\Omega\right)V_s=-r_o g_{ij}-\mathbf{G}_{UW}(N_{i,j},c)\mathbf{F}_W(c)\\&\quad-\mathbf{G}_{UU}(N_{i,j},\bar{s})\mathbf{F}_U(\bar{s})-\mathbf{G}_{UV}(N_{i,j},\bar{s})\mathbf{F}_V(\bar{s})-d_R^{(c)}\left(\mathrm{diag}\,(\mathbf{Q}_{RU})\left(N_{i,j}\right)-\mathrm{diag}\,(\mathbf{Q}_{RU})\left(N_{i_{ref}(j)+1,j}\right)\right)\end{aligned} \tag{59a}$$

$$\begin{aligned}&\mathbf{G}_{VU}(N_{i,j},s)\mathbf{F}_U(s)+\mathbf{G}_{VV}(N_{i,j},s)\mathbf{F}_V(s)+0\times V_s=-\mathbf{G}_{VW}(N_{i,j},c)\mathbf{F}_W(c)\\&\quad-\mathbf{G}_{VU}(N_{i,j},\bar{s})\mathbf{F}_U(\bar{s})-\mathbf{G}_{VV}(N_{i,j},\bar{s})\mathbf{F}_V(\bar{s})-d_R^{(c)}\left(\mathrm{diag}\,(\mathbf{Q}_{RV})\left(N_{i,j}\right)-\mathrm{diag}\,(\mathbf{Q}_{RV})\left(N_{i_{ref}(j)+1,j}\right)\right)\end{aligned} \tag{59b}$$

$$H\mathbf{1}^T(s)\mathbf{F}_U(s)+\mathbf{0}^T(s)\mathbf{F}_V(s)+0\times V_s=-T-r_o\left[\sin(\boldsymbol{\theta}(c))\sin(\boldsymbol{\phi}(c))\right]^T\mathbf{F}_W(c)-H\mathbf{1}^T(\bar{s})\mathbf{F}_U(\bar{s}) \tag{59c}$$

where the following quantities are defined for convenience:

$$g_{ij} = (i_{ref}(j) + 1 - i)\Delta\phi \ , \quad \text{and}$$
$$\mathbf{G}_{AB}(N_{i,j},:) = \mathbf{C}_{AB}(N_{i,j},:) - \mathbf{C}_{AB}(N_{i_{ref}(j)+1,j},:) \quad \text{for } A, B \in \{U, V, W\} \, .$$

As descried in further detail by Zéhil and Gavin (2013a), a "stick-slip" algorithm may be implemented, in combination with the "normal-contact" algorithm described in section (11), to solve system (59) while iterating on the subset of stick-contact nodes to satisfy the tangential boundary conditions given by (13).

14. Verification and application example

We consider the case of a hard sphere of radius $r_i = 20$ mm, coated with an incompressible viscoelastic layer of thickness $h = r_o - r_i = 1$ mm, and density $\rho = 1000$ kg/m^3, rolling in steady-state, without surface friction, on a rigid plane, at an angular speed $\Omega = 2.5$ rad/s. A vertical load $P = 100$ N is applied to the rolling sphere. The constitutive behavior of the viscoelastic coating is characterized by a single relaxation time $\tau = 0.125$ s. The short-term and long-term shear moduli are taken equal to $G_o = 6$ MPa and $G_\infty = 3$ MPa, respectively. We have chosen to present the simple case of a Standard Viscoelastic Solid, as is common practice in the relevant literature (e.g. Carbone and Putignano, 2013; Hunter, 1961; Persson, 2010; Qiu, 2006, 2009; Zéhil and Gavin, 2013c,a,b), for purposes of illustration and comparison. In fact, any linear viscoelastic solid would present the similar global trends of behavior, for instance, such as illustrated in figure 12. We are interested in determining the viscoelastic rolling resistance incurred by the sphere, as we vary some of the parameters specified above.

14.1. Verification of convergence

To optimize the computational costs related to building the boundary-element compliance matrices for the coating, an appropriate level of mesh refinement and a suitable truncation order are sought, based on convergence. To this aim, the resisting torque T_r is evaluated, in the conditions specified above, using an angular spacing between nodes $\Delta = \Delta\phi = \Delta\theta$ varying from $\pi/50$ rad to $\pi/400$ rad, and a truncation order $N_t = N_{t_\phi} = N_{t_\theta}$ ranging from 250 to 1500 terms. In evaluating expression (32) the integration domain $[r_i, r_o]$ is divided into $n_r = 50$ sub-intervals of equal amplitude. The resulting values of T_r are reproduced in table 2 and found to fall within 10% of each other. It is furthermore noted that, when the angular spacing between nodes is less than or equal to $\pi/250$ rad, the results are well within 0.6%, which corresponds to a satisfactory level of convergence. Table 2 confirms, as previously noted by Zéhil and Gavin (2013c,d) that the spatial mesh refinement has more impact on convergence than the truncation order. The "N/A" entries in this table correspond to cases where the number of Fourier terms retained in the series is insufficient to cover the 'bandwidth' taken by expression (38), or (53), at the specified level of refinement of the spatial mesh. Based on these observations, a nodal spacing of $\Delta\phi = \Delta\theta = \pi/250$ rad and a truncation order of $N_{t_\phi} = N_{t_\theta} = 500$ terms are retained for the purposes of this application example.

Δ	Truncation order N_t [Number of Terms]					
[rad]	250	500	750	1000	1250	1500
$\pi/50$	10.50	10.36	10.43	10.46	10.44	10.43
$\pi/75$	11.42	11.47	11.50	11.44	11.43	11.42
$\pi/100$	11.22	11.01	11.01	11.03	11.01	11.01
$\pi/150$	11.09	11.10	11.11	11.10	11.11	11.10
$\pi/200$	11.33	11.31	11.32	11.32	11.31	11.32
$\pi/250$	11.41	11.38	11.39	11.40	11.40	11.39
$\pi/300$	N/A	11.42	11.41	11.42	11.43	11.42
$\pi/350$	N/A	11.45	11.44	11.45	11.44	11.45
$\pi/400$	N/A	11.45	11.44	11.44	11.44	11.44

Table 2: Resisting torque T_r [mN.m]. Influence of spatial mesh refinement and truncation order on convergence.

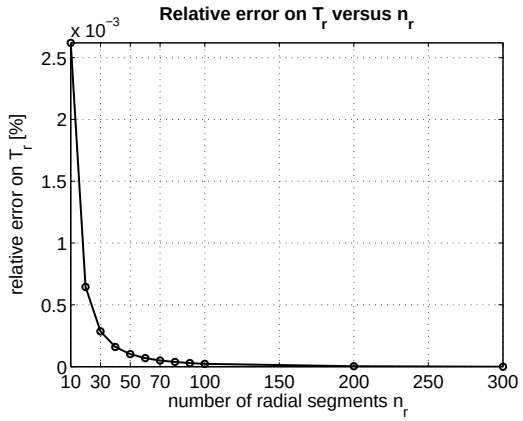

Figure 4: Influence of radial mesh fineness on convergence.

The relative error on the resisting torque T_r, evaluated with respect to the best available estimate of 11.44 mN.m, is plotted against the number of sub-intervals n_r in figure 4, for $\Delta = \pi/250$ rad and $N_t = 500$ Fourier terms. The error is well within 3.10^{-3}% for $n_r \geq 10$. The value of $n_r = 50$, retained in this example, is therefore deemed sufficient.

14.2. Verification of results

To verify that the steady-state model presented in this work yields accurate results, a three-dimensional finite element model of the same physical system is implemented under ABAQUS and rolling contact simulations are run, in implicit dynamic analyses, at prescribed angular velocities, until a steady-state rolling resistance is reached. To limit the computational cost of the temporal finite element simulations, the modeling of the viscoelastic coating is limited to a strip, rigidly tied to the sphere, as illustrated in figure 5. The width of the strip is chosen so as to contain the largest area of influence of the contact interactions, characterized by stresses and strains in the continuum of the coating of the same order of magnitude as the contact fields.[1] Due to material incompressibility, a hybrid formulation is used to avoid volumetric locking (e.g. Hughes, 2000): the strip is discretized using 10-node quadratic tetrahedra, with constant pressure. The mesh parameter (element size) is set to approximately one third of the layer's thickness. Inertial forces and geometric nonlinearities are accounted for in the solution scheme (e.g. Zienkiewicz and Taylor, 2005), and surface-to-surface normal contact is implemented using the "hard" contact pressure-overclosure relationship.

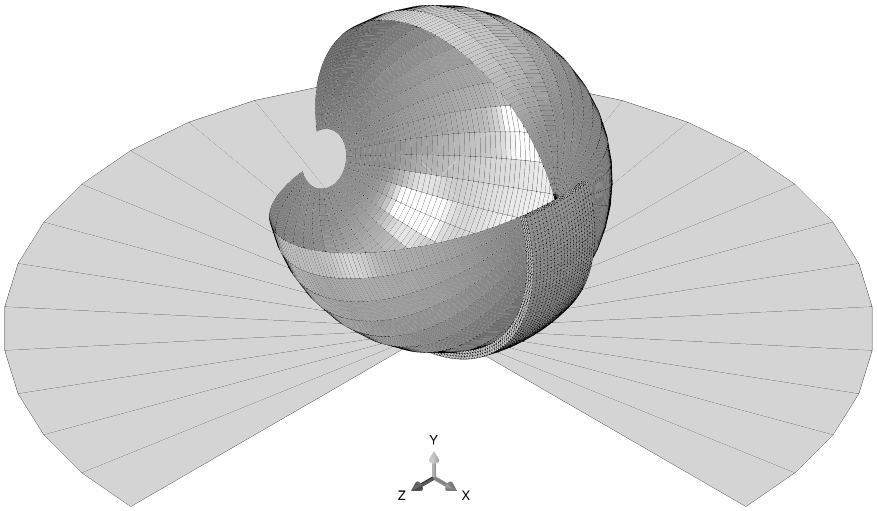

Figure 5: Finite element model under ABAQUS: rigid sphere coated with a viscoelastic strip, rolling on a rigid plane.

Figure 6 shows the time-history of the resisting torque T_r for several simulations run at different angular speeds Ω, ranging between 0.5 rad/s and 4.0 rad/s. In each simulation, the prescribed rolling speed is applied instantaneously, as a boundary condition on the rigid sphere. Shorter integration time-steps are used at larger velocities. The simulations are interrupted once a stead-state in rolling contact is reached.

The steady-state rolling resistance is then evaluated using the three-dimensional boundary element formulation and the contact solving strategy proposed in this work, for angular velocities ranging from 0.05 rad/s to 25 rad/s. Steady-state results from both the proposed model and the finite element model are compared in figure 7 which shows that they are in very good agreement. Indeed, despite the various sources of uncertainty in the predictions of both models, such as approximations in geometry, numerical errors related to both spatial and temporal discretizations, truncation errors, and the uncertainty associated with the detection of a steady-state in the finite element simulation, all the numerical values are well within 5% of each other.

[1] For verification purposes, a finite element simulation is run at a rolling speed of $\Omega = 0.3$ rad/s, which corresponds roughly to the deepest penetration, with a strip of double the retained width. The difference in rolling resistance is found to be less than 0.1%.

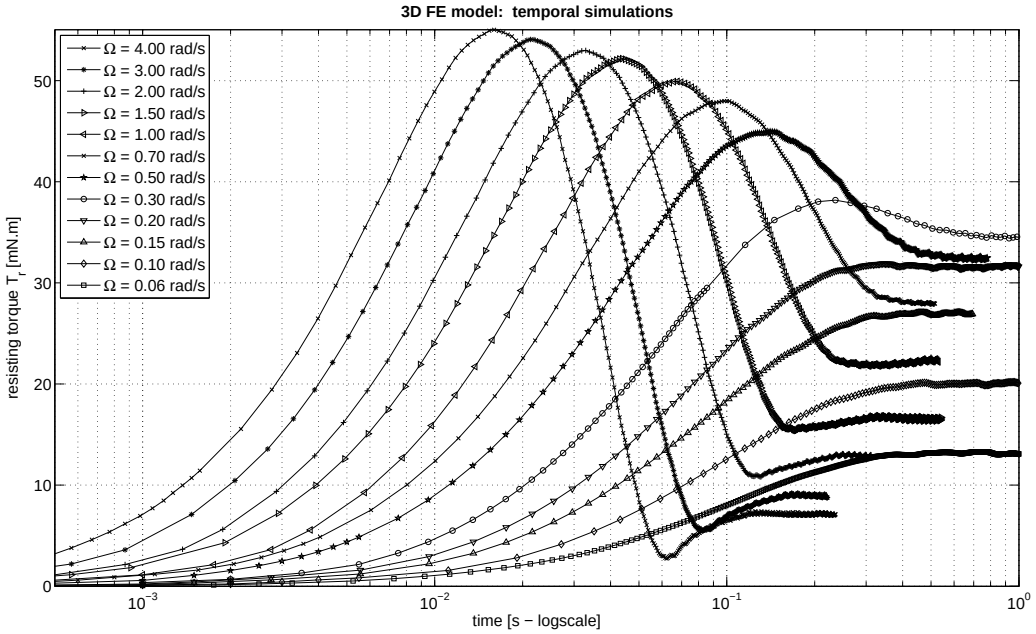

Figure 6: Finite element simulations at prescribed rolling speeds, without surface friction: time-history of the resisting torque.

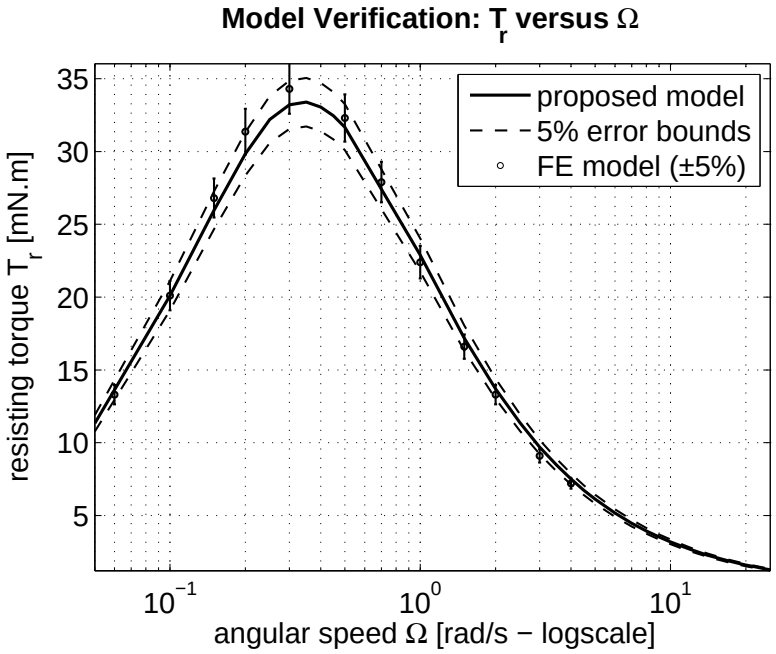

Figure 7: Model verification: rolling resistance results are in good agreement with finite element simulations.

14.3. Influence of surface friction

Surface friction of the Coulomb type is added to the finite element model described in section 14.2. Several simulations are performed at the same prescribed angular speed $\Omega = 0.2$ rad/s, but with different values of the coefficient of surface friction μ in the interval $[0, 2]$. The time-histories of the resisting torque T_r are plotted, for each value of μ, in figure 8. It may be noted that the difference (overshoot) between the peak value of T_r during the transient and its final value in steady-state increases with μ.

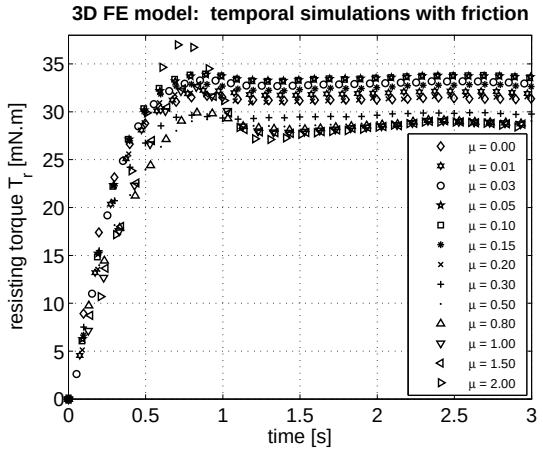

Figure 8: Frictional finite element simulations, performed at a constant angular speed $\Omega = 0.2$ rad/s, prescribed instantaneously at $t = 0$ s, for different values of the coefficient of surface friction μ, varying between 0 and 2. To improve the clarity of the plot, only 5% of the time integration points are shown. The overshoot is an increasing function of μ.

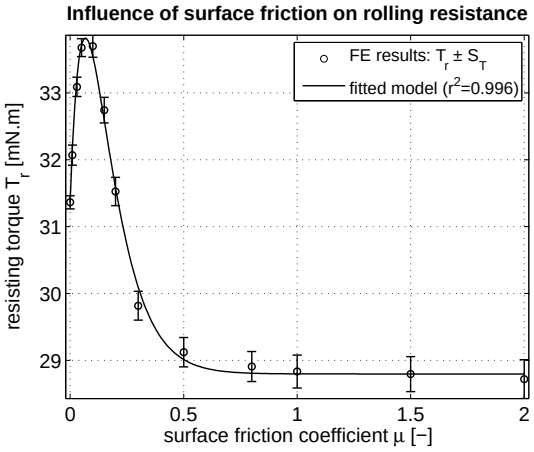

Figure 9: Influence of the coefficient of surface friction μ on steady-state values of the resisting torque T_r. The behavior of $T_r(\mu)$ is characterized by a left boundary layer of width $\epsilon_\mu \approx 0.1$. Slipping friction is dominant in the inner domain ($\mu \leq \epsilon_\mu$). The influence of contact shear stresses on the offset of the vertical resultant is dominant in the outer domain ($\mu > \epsilon_\mu$).

Numerical errors originating from the finite element model generate a moderate waviness in the time histories of T_r, even in steady-state. The resulting uncertainty is accounted for by computing a mean steady-state value of $T_r(\mu)$ and a standard deviation $S_{T_r}(\mu)$ from the samples of data corresponding to $t \geq 2$ seconds. These finite element results are plotted against μ in figure 9. Qualitatively, from the pattern taken by the data points, which reveals a left boundary layer of width $\epsilon_\mu \approx 0.1$ (see e.g. Logan, 2006), it is clear that the behavior of $T_r(\mu)$ is driven by two competing mechanisms, each dominant in a given range of the parameter μ:

(i) for relatively small values of the friction coefficient, i.e. $\mu \leq \epsilon_\mu$, the maximum contact shear stresses are small. Their influence on the normal contact stress field, and on the viscoelastic rolling friction, is therefore negligible. On the other hand, because the slipping thresholds are low, slipping occurs on large portions of the contact surface, which results in energy losses from surface friction that are relatively significant. The overall frictional resistance to rolling is hence larger than the purely viscoelastic resistance, computed without friction,

(ii) for relatively large values of the friction coefficient, i.e. $\mu > \epsilon_\mu$, the slipping thresholds are large and most of the contact surface sticks to the plane. The contribution of slipping friction to rolling resistance is therefore negligible. On the other hand, because contact shear stresses are relatively large, their influence on the distribution of normal contact stresses, which reduces the offset of the vertical resultant $-P$, is significant. The overall frictional resistance to motion therefore decreases in comparison to that computed in the absence of surface friction.

This brief discussion on the governing mechanisms of rolling resistance is interesting. However, from a quantitative point of view, the influence of μ on T_r is limited. Indeed, as can be seen in figure 9, all computed values of the resisting torque are roughly within 15% of each other. Furthermore, if the localized peak in $T_r(\mu)$ corresponding to the narrow left boundary-layer is disregarded, rolling resistance decreases no more than 8.5% with added surface friction. The dependence of T_r on μ may be fitted in four steps:

	$H = 1$ mm	$H = 5$ mm
r^2	≈ 1	≈ 1
$a_{p,max}$	5.037×10^{-5}	2.321×10^{-5}
$a_{p,min}$	4.766×10^{-5}	2.097×10^{-5}
$b_{p,max}$	1.430	1.368
$b_{p,min}$	1.418	1.344

Table 3: Fitting coefficients for $T_r(P)$ [N.m] corresponding to 95% confidence intervals (r is the multiple correlation coefficient).

	$P = 25$ N	$P = 50$ N	$P = 75$ N	$P = 100$ N
r^2	0.9999	0.9999	0.9999	0.9999
$a_{h,max}$	0.677×10^{-2}	2.018×10^{-2}	3.811×10^{-2}	5.972×10^{-2}
$a_{h,min}$	0.670×10^{-2}	1.997×10^{-2}	3.770×10^{-2}	5.895×10^{-2}
$b_{h,max}$	78.446	71.332	67.310	64.205
$b_{h,min}$	69.702	64.898	61.842	58.431
$c_{h,max}$	0.827	0.835	0.840	0.842
$c_{h,min}$	0.809	0.821	0.827	0.828

Table 4: Fitting coefficients for $T_r(h)$ [N.m] corresponding to 95% confidence intervals (r is the multiple correlation coefficient).

(i) an 'inner' model $T_{r,i}(\mu)$ operating on the scaled variable μ/ϵ_μ is chosen to apply inside of the left boundary layer, i.e. for small values of the independent variable μ. An exponential model is retained in this case

$$T_{r,i}(\mu) = a_i \left(1 + b_i \left(1 - e^{-\frac{(\mu/\epsilon_\mu)}{c_i}}\right)\right), \tag{60}$$

where a_i, b_i and c_i are parameters of the inner model. The first parameter a_i is in fact fixed, since $a_i = T_r(\mu = 0)$.

(ii) an 'outer' model $T_{r,o}(\mu)$ is chosen to apply outside of the left boundary layer, i.e. for larger values of μ. A model of the exponential form, with parameters a_o, b_o and c_o, is retained as well

$$T_{r,o}(\mu) = a_o \left(1 + b_o e^{-\frac{\mu}{c_o}}\right). \tag{61}$$

(iii) the limit of the inner model is matched to the limit of the outer model at the intermediate scale characterized by the variable $\eta = \mu/\sqrt{\epsilon_\mu}$. This is done as follows

$$\delta = \lim_{\epsilon_\mu \to 0} T_{r,i}\left(\sqrt{\epsilon_\mu}\eta\right) = \lim_{\epsilon_\mu \to 0} T_{r,o}\left(\sqrt{\epsilon_\mu}\eta\right) \quad \Rightarrow \quad a_i(1 + b_i) = a_o(1 + b_o). \tag{62}$$

(iv) a uniformly valid model $T_{r,u}(\mu)$ is obtained by adding the inner model to the outer model and subtracting their common intermediate-scale limit δ

$$T_{r,u}(\mu) = T_{r,i}(\mu) + T_{r,o}(\mu) - \delta. \tag{63}$$

The model $T_{r,u}$, which has four independent parameters a_o, b_o, c_o, and c_i, is fitted to the finite element results, as shown in figure 9.

14.4. Influence of the applied load

To date, there are no closed-form expressions for the rolling resistance of a viscoelastic sphere on rigid plane that reflects the nonlinear dependence on the load P. As an alternative, we consider for guidance, an approximate closed-form expression for the rolling resistance incurred by a rigid sphere rolling on a viscoelastic half-space, as derived by Greenwood and Tabor (1958) who integrated, under the small strain assumption, the horizontal projection of the stationary normal stress distribution, as given by Hertz (1881), over the front half of the contact disk. The resisting torque corresponding to this formulation may be written as follows

$$T_r \approx \left(\frac{3^4 (1 - \nu) R P^4}{2^{15} G}\right)^{\frac{1}{3}}, \tag{64}$$

where G is the shear modulus and ν corresponds to Poisson's ratio. Expression (64) does not reflect the dependence of rolling resistance on velocity. However, according to (64), T_r depends on P raised at the power $4/3$. It is interesting to know whether the more accurate rolling resistance estimates given by the model proposed in this work show the same dependence on P. To this aim, the resisting torque T_r is plotted, in the context of our example, against the vertical load P, which ranges between 10 N and 100 N, in figures 10(a) and 10(b), for $h = 1$ mm and $h = 5$ mm, respectively. Rolling resistance clearly increases with the applied load, and it does so unboundadly. As can be seen on figures 10(a)

and 10(b), the dependence of T_r on P is well fitted by power laws of the form $T_r(P) = a_p P^{b_p}$ (solid lines). The dashed lines correspond to 95% confidence intervals on the fits. The parameter bounds corresponding to the same level of confidence are given in table 3. It can be observed that the values taken by the parameter b_p are close, but not equal, to the value of $4/3$ given by expression (64). In fact, b_p appears to be larger than $4/3$ and to decrease with increasing h, i.e. as the coating becomes thicker and the systems tends towards a *solid* viscoelastic sphere.

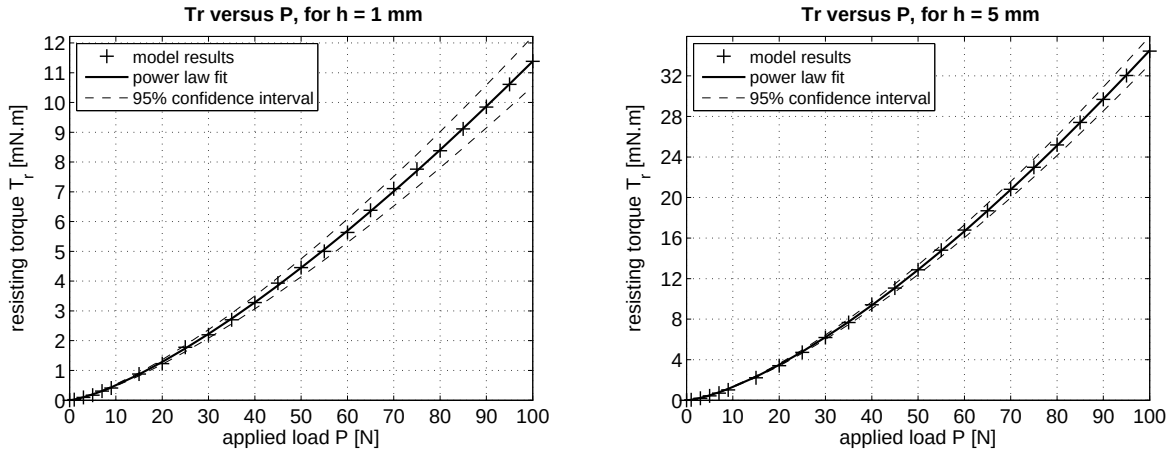

(a) $h = 1$ mm (b) $h = 5$ mm

Figure 10: Influence of the applied load on the resisting torque for $h = 1$ mm, and $h = 5$ mm.

14.5. Influence of coating thickness

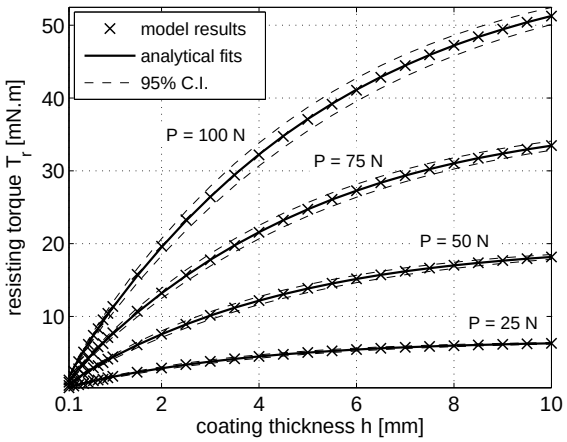

Figure 11: Influence of layer thickness on the resisting torque, at fixed $r_o = 21$ mm, for $P = 25$ N, 50 N, 75 N, and 100 N.

The resisting torque T_r is plotted in figure 11 against coating thickness in the range $0.1 \leq h \leq 10$ mm, at fixed $r_o = 21$ mm, for $P = 25$ N, 50 N, 75 N, and 100 N. The dependence of rolling resistance on h is comparable, from a qualitative point of view, to that incurred by a hard cylinder (e.g Qiu, 2006) or by a hard sphere (e.g Zéhil and Gavin, 2013c) rolling on a viscoelastic layer attached to a plane rigid subbase: the resisting toque increases with h and tends towards a limiting value which, in the present case, corresponds to that incurred by a *solid* viscoelastic sphere

rolling on a rigid plane. This dependence is well fitted by three-parameter composite sigmoidal-power-law functions of the form $T_r(h) = a_h \tanh(b_h h^{c_h})$, which correspond to the solid lines in figure 11. The dashed lines reflect the 95% confidence intervals on the fits. The 95% confidence intervals on the fitted parameters are given in table 4.

14.6. Influence of rolling speed

The influence of rolling speed on the resisting torque is shown in figures 12(a) and 12(b) for a coating thickness of $h = 1$ mm and $h = 5$ mm, respectively. The different curves plotted on these figures correspond to equally spaced values of the applied load P, ranging from 10 N to 100 N. To understand the dependence of rolling resistance on velocity, it is useful to recall that the frequency-dependent viscoelastic master-curves of a linear viscoelastic material can be written in the form of a Prony series, i.e.

$$G'(\omega) = G_o\left(g_\infty + \sum_{k=1}^{n} \frac{g_k \omega^2 \tau_k^2}{1+\omega^2\tau_k^2}\right) \qquad \text{(storage modulus)}, \tag{65a}$$

$$G''(\omega) = G_o \sum_{k=1}^{n} \frac{g_k \omega \tau_k}{1+\omega^2\tau_k^2} \qquad \text{(loss modulus)}, \tag{65b}$$

where ω is the angular frequency, the material parameters τ_k correspond to internal relaxation times, and the associated weights g_k satisfy

$$g_\infty + \sum_{k=1}^{n} g_k = 1. \tag{66}$$

The loss modulus $G''(\omega)$ reflects the amount of dissipated energy at a given frequency ω. In relation to the material's distribution of internal time-scales, when the rolling occurs at a relatively low speed, the forcing frequencies tend to zero, and so does the loss modulus. Alternatively, at a relatively large rolling velocity, the forcing frequencies tend to infinity and $G''(\omega)$ also vanishes. In such conditions, the material behaves almost elastically, regardless of the applied load P. The loss modulus reaches a peak at an intermediate rolling speed, which depends on the material's parameters. The material parameters retained in this example were stated at the beginning of section 14. These correspond to $G_o = 6$ MPa, $n = 1$, $g_\infty = g_1 = 0.5$, and $\tau_1 = 0.125$ s.

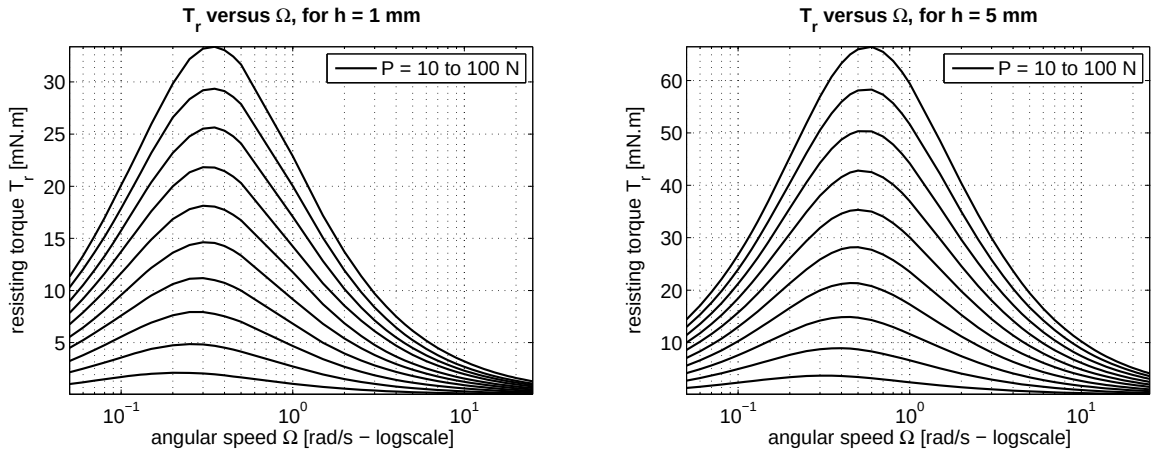

(a) $h = 1$ mm (b) $h = 5$ mm

Figure 12: Influence of rolling speed on the resisting torque, for $h = 1$ mm, and $h = 5$ mm.

It is here assumed that the sphere's coating does not heat significantly because of the motion. In general, this is justified under certain assumptions, such as: (i) small activation energy, (ii) small loss factor, (iii) small deformations, (iv) limited slipping and/or surface friction at the contact interface, (v) moderate velocity, (vi) coating of limited thickness, (vii) low specific heat capacity, and (viii) favorable conditions of heat dissipation, so as to limit the accumulation

of thermal energy in the coating. It is interesting to note that rolling resistance is usually governed by material properties in a limited range of relevant frequencies, depending on the rolling speed. At higher velocities, this range is shifted towards higher frequencies, thus partially compensating the shift incurred by frequency-domain master-curves due to a moderate increase in temperature.

14.7. Influence of inertial effects

A simple dimensional analysis reveals that inertial effects can be related by the following dimensionless group, of which rolling resistance is a function:

$$\Pi = \frac{\rho \Omega^2 r_i^2}{G_o}. \tag{67}$$

By analogy to a single degree-of-freedom oscillator, the dimensionless group Π may be interpreted as the square of the ratio of a 'forcing' frequency Ω (i.e. the rolling speed) to a 'natural' frequency Ω_n given by

$$\Omega_n = \sqrt{\frac{G_o}{\rho r_i^2}}. \tag{68}$$

The influence of inertial effects on the resisting torque, and on the plane's penetration into the sphere's coating, are illustrated in figure 13, which shows a sharp increase in penetration, and in rolling resistance, as Ω approaches Ω_n. The numerical value taken by Π in the example treated in this section is of the order of 10^{-7}, which is very small compared to 1. At moderate velocities, with typical material properties, and unless the rolling object is exceptionally large, Π is small, and the influence of inertial effects is rather limited. Getting Π closer to 1 by increasing the density, with all other quantities remaining equal would be of course unrealistic. This is especially true as material stiffness usually increases with density. However, one can imagine applications where Π would approach the value of 1, for instance, due to high velocities, such in transportation, industry, and defense.

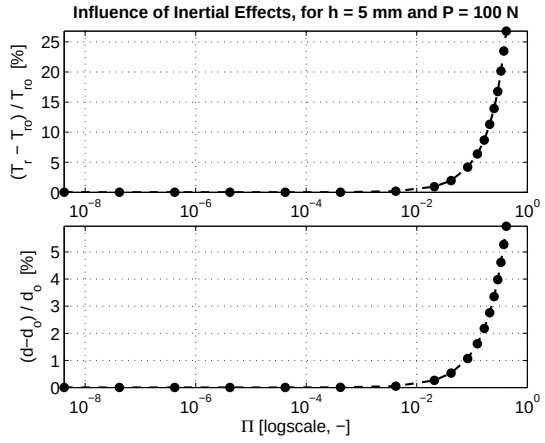

Figure 13: Influence of inertial effects on the resisting torque T_r, and on the penetration $d = r_o - H$, for $h = 5$ mm, and $P = 100$ N. The quantities T_{ro} and d_o corresponding to zero density ($\rho = 0$) are taken as reference.

15. Conclusions

A full three-dimensional boundary element formulation of a multi-layered viscoelastic coating covering a hard spherical core rotating in steady-state is presented in this work. This formulation accommodates an arbitrary number of layers, each layer being of arbitrary thickness. It incorporates the viscoelastic and inertial effects of steady-state motion, including the Coriolis effect. Linear viscoelastic materials are characterized, in the most general way, by their frequency-domain master-curves, which enables the implementation of as many rates of internal dissipation as

necessary to model their actual behavior. The proposed formulation relates two-dimensional Fourier series expansions of surface displacements and stresses. Based on these relations, a compliance matrix is constructed, in the spatial domain, by discretizing the outer boundary of the deformable coating into nodes. The computational cost of building such a compliance matrix is optimized, based on configurational similarities and symmetry.

This numerical model, which fully characterizes the mechanical behavior of the coating's outer boundary, can be used in diverse problem settings, at various scales, and in different fields, such as modeling important aspects in the behavior of interacting nano-particles, biological organisms, particles, grains or pellets in granular materials, bones in articulations, spherical components in industrial machines, transport vehicles, satellites and robots, or in risk mitigation devices such as rolling isolation platforms.

In this work, the proposed formulation was applied, in combination with a rolling contact solving strategy, to evaluate the resistance to motion incurred by a hard sphere, coated with a viscoelastic layer, as it is rolling on a rigid plane. Steady-state results generated by the proposed model were verified by comparison to those obtained from running dynamic simulations on a three-dimensional finite element model of a coated sphere, rolling on a rigid plane, beyond the transient. A detailed application example included a verification of convergence and illustrated the dependence of the resisting torque on various parameters, such as the applied load, the thickness of the coating, and the rolling velocity.

Appendix A. Two-variable periodicity of physical fields

Consider a generic physical field $\hat{f}(r, \phi, \theta)$ in the continuum of the sphere's viscoelastic coating, where the spherical coordinates r, ϕ and θ designate the radius, the azimuth (or longitude) and the inclination (or latitude), respectively. The vertical projection of the sphere's center-point C onto the hard plane corresponds to the angular coordinates $\phi = \pi/2$ and $\theta = \pi/2$. In practice, contact occurs for values of ϕ and θ over a small surface in the neighborhood of $\pi/2$.

The azimuth ϕ belongs to the interval $]-\pi, +\pi]$. The function of the single variable ϕ denoted by $\hat{f}_{r,\theta}(\phi) = \hat{f}(r, \phi, \theta)$, for fixed values of r and θ, can be extended to a 2π-periodic function in ϕ over the real line $\mathbb{R}$, by defining $f_{r,\theta}(\phi + 2k\pi) = \hat{f}_{r,\theta}(\phi)$ for any $\phi \in]-\pi, +\pi]$ and any integer k.

The latitude θ belongs to the interval $[0, +\pi]$. The function of the single variable θ denoted by $\hat{f}_{r,\phi}(\theta) = \hat{f}(r, \phi, \theta)$ for fixed values of r and ϕ can be extended to a 2π-periodic function in θ over $\mathbb{R}$, in two steps:

(i) from $[0, +\pi]$ to $]-\pi, +\pi]$, by defining

$$\tilde{f}_{r,\phi}(\theta) = \begin{cases} \hat{f}_{r,\phi}(\theta), & \text{for } \theta \in [0, +\pi], \\ 0, & \text{for } \theta \in]-\pi, 0[, \end{cases} \tag{A.1}$$

(ii) then, from $]-\pi, +\pi]$ to $\mathbb{R}$: by defining $f_{r,\phi}(\theta + 2k\pi) = \tilde{f}_{r,\phi}(\theta)$ for any $\theta \in]-\pi, +\pi]$ and any integer k.

For any admissible value of the variable r, the functions $f_{r,\theta}(\phi)$ with $\phi \in \mathbb{R}$, and $f_{r,\phi}(\theta)$ with $\theta \in \mathbb{R}$, are the restrictions to constant ϕ, and constant θ, respectively, of the 2π-periodic function $f(r, \phi, \theta)$ in the two variables ϕ and θ, which is addressed in section 5.

Appendix B. In-depth justification of the geometric approximation

The simplifying assumption retained in section 6 is necessary to overcome significant complications associated with the dependence of certain coefficients in equations (8) and (9) on the spatial variable θ. Indeed, the simplest terms, such as $\sin(\theta)$ and $\cos(\theta)$ introduce a coupling between Fourier series coefficients of neighboring order in m and n. To show this fact, we consider, for simplicity, the following equation involving two fields $f(r, \phi, \theta)$ and $g(r, \phi, \theta)$

$$f(r, \phi, \theta) - \sin(\theta)\, g(r, \phi, \theta) = 0. \tag{B.1}$$

Applying the aforementioned transformation procedure to equation (B.1) yields

$$f_{pq}(r) - \sum_{n=-\infty}^{\infty} g_{pn}(r) \frac{1}{2\pi} \int_{-\pi}^{\pi} \sin(\theta)\, e^{in\theta} e^{-iq\theta} d\theta = f_{pq}(r) + \frac{i}{2}\left(g_{p(q-1)}(r) - g_{p(q+1)}(r)\right) = 0. \tag{B.2}$$

Hence, equation (B.1) in the spatial domain transforms into an equation (i.e. B.2) relating the Fourier coefficient f_{mn} of field $f(r,\phi,\theta)$ to the Fourier coefficients $g_{m(n-1)}$ and $g_{m(n+1)}$ of field $g(r,\phi,\theta)$, which are of different order. Other terms such as $1/\sin(\theta)$ and $\cot(\theta)$ lead to non-converging integrals. We consider, for instance, the following integral in $\cot(\theta)$, which arises when the transformation procedure is applied to equations (8b), (8c) or (9f)

$$\frac{1}{2\pi}\int_{-\pi}^{\pi}\cot(\theta)\,e^{i(n-q)\theta}d\theta. \tag{B.3}$$

Expression (B.3) does not correspond to a finite quantity. Nevertheless, provided that the fields generated by the Coriolis effect are small in comparison witch those due to contact (see equation (8a)), the function $\cot(\theta)$ may be restricted as follows

$$\overline{\cot}(\theta)=\begin{cases}\cot(\theta), & \text{if } \theta\in\left[\frac{\pi}{2}-\beta,\frac{\pi}{2}+\beta\right],\\ 0, & \text{otherwise,}\end{cases} \tag{B.4}$$

where the dihedral angle 2β is taken sufficiently large so that all fields are negligible outside of the interval $[\pi/2-\beta,\pi/2+\beta]$. With these assumptions, expression (B.3) becomes

$$\frac{1}{2\pi}\int_{-\pi}^{\pi}\overline{\cot}(\theta)\,e^{i(n-q)\theta}d\theta=\frac{1}{2\pi}\int_{\pi/2-\beta}^{\pi/2+\beta}\cot(\theta)\,e^{i(n-q)\theta}d\theta, \tag{B.5}$$

which is convergent. Unfortunately, it turns out that the Fourier series expansion of expression (B.4) has an infinite number of terms. Thus, despite the restriction proposed in (B.4), terms such as $\cot(\theta)$ generate a coupling between Fourier series coefficients of different order in m and n, involving an infinite number of terms.

Appendix C. Transformation of constitutive equation into the Fourier domain

The constitutive equations are handled as follows: Fourier series expansions (14) of stresses and strains are plugged into equation (10) and all terms in the latter are shifted to the left-hand-side

$$\begin{aligned}\sum_{m,n=-\infty}^{\infty}\sigma_{ij_{mn}}(r)\,e^{im\phi}e^{in\theta}-\int_{-\infty}^{\infty}2\mu(t-\tau)\frac{\partial}{\partial\tau}\left(\sum_{m,n=-\infty}^{\infty}\epsilon_{ij_{mn}}(r)\,e^{im\phi}e^{in\theta}\right)d\tau\\ -\delta_{ij}\int_{-\infty}^{\infty}\lambda(t-\tau)\frac{\partial}{\partial\tau}\left(\sum_{m,n=-\infty}^{\infty}\epsilon_{kk_{mn}}(r)\,e^{im\phi}e^{in\theta}\right)d\tau=0.\end{aligned} \tag{C.1}$$

Equation (2) is then used to reveal the time variable explicitly

$$\begin{aligned}\sum_{m,n=-\infty}^{\infty}\sigma_{ij_{mn}}(r)\,e^{im\phi'}e^{in\theta'}e^{im\Omega t}-\int_{-\infty}^{\infty}2\mu(t-\tau)\frac{\partial}{\partial\tau}\left(\sum_{m,n=-\infty}^{\infty}\epsilon_{ij_{mn}}(r)\,e^{im\phi'}e^{in\theta'}e^{im\Omega\tau}\right)d\tau\\ -\delta_{ij}\int_{-\infty}^{\infty}\lambda(t-\tau)\frac{\partial}{\partial\tau}\left(\sum_{m,n=-\infty}^{\infty}\epsilon_{kk_{mn}}(r)\,e^{im\phi'}e^{in\theta'}e^{im\Omega\tau}\right)d\tau=0.\end{aligned} \tag{C.2}$$

Partial differentiation with respect to time is performed and terms are rearranged under the same summation sign so that complex exponentials in ϕ' and θ' are factored out

$$\sum_{m,n=-\infty}^{\infty}\left[\sigma_{ij_{mn}}(r)\,e^{im\Omega t}-im\Omega\int_{-\infty}^{\infty}2\mu(t-\tau)\,e^{im\Omega\tau}d\tau\epsilon_{ij_{mn}}(r)-\delta_{ij}im\Omega\int_{-\infty}^{\infty}\lambda(t-\tau)\,e^{im\Omega\tau}d\tau\epsilon_{kk_{mn}}(r)\right]e^{im\phi'}e^{in\theta'}=0, \tag{C.3}$$

after which the orthogonality of complex exponentials is invoked to eliminate the summation sign

$$\sigma_{ij_{mn}}(r)\,e^{im\Omega t}-im\Omega\int_{-\infty}^{\infty}2\mu(t-\tau)\,e^{im\Omega\tau}d\tau\epsilon_{ij_{mn}}(r)-\delta_{ij}im\Omega\int_{-\infty}^{\infty}\lambda(t-\tau)\,e^{im\Omega\tau}d\tau\epsilon_{kk_{mn}}(r)=0. \tag{C.4}$$

The change of variable $\xi=t-\tau$ is then introduced, and the complex exponential in the variable t is factored out

$$\left[\sigma_{ij_{mn}}(r)-im\Omega\int_{-\infty}^{\infty}2\mu(\xi)\,e^{-im\Omega\xi}d\xi\epsilon_{ij_{mn}}(r)-\delta_{ij}im\Omega\int_{-\infty}^{\infty}\lambda(\xi)\,e^{-im\Omega\xi}d\xi\epsilon_{kk_{mn}}(r)\right]e^{im\Omega t}=0. \tag{C.5}$$

Equation 20 is readily deduced from the fact that the above is true for all times t.

Acknowledgments

The authors wish to thank Professor Wilkins Aquino for providing access to valuable computational resources that were instrumental in verifying numerical results presented in this work.

This material is based upon work supported by the National Science Foundation under Grant No. NSF-CMMI-0900324. Any opinions, findings, and conclusions or recommendations expressed in this material are those of the authors and do not necessarily reflect the views of the National Science Foundation.

References

Arnold, J. W., 1985. Predicting vibratory sorting probability of viscoelastic spheres. M.S. dissertation, Ohio State University.
URL http://rave.ohiolink.edu/etdc/view?acc_num=osu1203374975

Atsbha, H., 1993. Viscoelastic flows around spheres. M.A.S. dissertation, University of Ottawa.
URL http://search.proquest.com/docview/304082622?accountid=10598

Bahadur, S., Schwartz, C. J., 2008. Tribology of Polymeric Nanocomposites. Vol. 55 of Tribology and Interface Engineering Series. Elsevier.
URL http://www.sciencedirect.com/science/article/pii/S1572336408550026

Bambusi, D., Haus, E., 2012. Asymptotic stability of synchronous orbits for a gravitating viscoelastic sphere. Celestial Mechanics and Dynamical Astronomy 114 (3), 255–277.
URL http://dx.doi.org/10.1007/s10569-012-9438-7

Berg, M. A., 1999. A viscoelastic continuum model of nonpolar solvation. iii. electron solvation and nonlinear coupling effects. The Journal of Chemical Physics 110 (17), 8577–8588.
URL http://link.aip.org/link/?JCP/110/8577/1

Bir, C. A., Resslar, M., Stewart, S., 2012. Skin penetration surrogate for the evaluation of less lethal kinetic energy munitions. Forensic Science International (Online) 220 (1), 126–129.
URL http://search.proquest.com/docview/1036661712?accountid=10598

Bogy, D. B., 1968. Edge-bonded dissimilar orthogonal elastic wedges under normal and shear loading. Journal of Applied Mechanics 35 (3), 460–466.
URL http://dx.doi.org/10.1115/1.3601236

Bose, S., Das, S. K., Karp, J. M., Karnik, R., 12 2010. A semianalytical model to study the effect of cortical tension on cell rolling. Biophysical journal 99 (12), 3870–3879.
URL http://linkinghub.elsevier.com/retrieve/pii/S0006349510013263

Brilliantov, N. V., Pöschel, T., 1998. Rolling friction of a viscous sphere on a hard plane. Europhysics Letters 42, 511–516.

Bueche, A. M., Flom, D. G., 1959. Surface friction and dynamic mechanical properties of polymers. Wear 2, 168–182.

Carbone, G., Putignano, C., 2013. A novel methodology to predict sliding and rolling friction of viscoelastic materials: Theory and experiments. Journal of the Mechanics and Physics of Solids 61 (8), 1822 – 1834.
URL http://www.sciencedirect.com/science/article/pii/S0022509613000604

Chertok, D. L., Golden, J. M., Graham, G. A. C., 2001. Hysteretic friction for the transient rolling contact problem of linear viscoelasticity. Journal of Applied Mechanics 68 (4), 589–595.

Coghill, P. A., 2012. The role of cell deformation during selectin-mediated neutrophil rolling. Ph.D. dissertation, University of Oklahoma.
URL http://search.proquest.com/docview/1027594929?accountid=10598

Coulomb, C., 1821. Théorie des machines simples: en ayant égard au frottement de leurs parties et à la roideur des cordages. Bachelier.

Eakasit, S., Gunasekaran, S., Lakes, R. S., 2009. Broadband viscoelastic spectroscopy: A new technique for characterizing rheological behavior of solid foods. International Journal of Food Properties 12 (1), 102–113.
URL http://www.tandfonline.com/doi/abs/10.1080/10942910802223388

Els, D. N. J., 2009. The effectiveness of particle dampers under centrifugal loads. Ph.D. dissertation, University of Stellenbosch.
URL http://hdl.handle.net/10019.1/1429

Esat, I. I., Ozada, N., 2 2010. Articular human joint modelling. Robotica 28, 321–339.
URL http://journals.cambridge.org/article_S0263574709990592

Flom, D. G., 1960. Rolling friction of polymeric materials. i. elastomers. Journal of Applied Physics 31 (2), 306–314.

Flom, D. G., Bueche, A. M., 1959. Theory of rolling friction for spheres. Journal of Applied Physics 30 (11), 1725–1730.

Flügge, W., 1975. Viscoelasticity. Springer-Verlag.

Galin, L., Gladwell, G., 2008. Contact Problems: The Legacy of L.A. Galin. Solid Mechanics and Its Applications. Springer.

Golden, J., Graham, G., 2001. The problem of a viscoelastic cylinder rolling on a rigid half-space. Mathematical and Computer Modelling 34 (12–13), 1363–1397.

Greenwood, J. A., Minshall, H., Tabor, D., 1961. Hysteresis losses in rolling and sliding friction. Proceedings of the Royal Society of London. Series A, Mathematical and Physical Sciences 259 (1299), 480–507.

Greenwood, J. A., Tabor, D., 1958. The friction of hard sliders on lubricated rubber: The importance of deformation losses. Proceedings of the Physical Society 71 (6), 989.

Hall, D. E., 2001. Fundamentals of rolling resistance. Rubber Chemistry and Technology 74 (3), 525–525.

Harvey, Jr., P. S., Gavin, H. P., 2013. An experimentally-validated simplified model of a rolling isolation system. Earthquake Engineering and Structural Dynamics (in review).

Harvey, Jr., P. S., Zéhil, G.-P., Gavin, H. P., 2013. Damped rolling isolation: theory and experiments. (in preparation).

Hertz, H., 1881. Über die berührung fester elastischer körper (on contact between elastic bodies). Journal für die reine und angewandte Mathematik 92, 156–171.

Hughes, T., 2000. The finite element method: linear static and dynamic finite element analysis. Dover Civil and Mechanical Engineering Series. Dover Publications.
URL http://store.doverpublications.com/0486411818.html

Hunter, S., 1961. The rolling contact of a rigid cylinder with a viscoelastic half space. Journal of Applied Mechanics 28 (4), 611–617.

Hunter, S. C., 5 1968. The motion of a rigid sphere embedded in an adhering elastic or viscoelastic medium. Proceedings of the Edinburgh Mathematical Society (Series 2) 16, 55–69.
URL http://journals.cambridge.org/article_S0013091500012189

Johnson, K., 1985. Contact mechanics. Cambridge University Press, Cambridge.

Kumar, P., Sarkar, D., Gupta, S. C., 1988. Rolling resistance of elastic wheels on flat surfaces. Wear 126 (2), 117 – 129.
URL http://www.sciencedirect.com/science/article/pii/0043164888901330

Kuznetsov, Y., 1978. The superposition principle in the solution of contact friction stress problems. Wear 50 (1), 183 – 189.
URL http://www.sciencedirect.com/science/article/pii/0043164878902557

Lakes, R., 2009. Viscoelastic Materials. Cambridge University Press.

Lakes, R. S., 2004. Viscoelastic measurement techniques. Review of Scientific Instruments 75 (4), 797–810.
URL http://link.aip.org/link/?RSI/75/797/1

Langus, J., Sustaric, P., Rodic, T., 2011. Impact response of polymer-coated grinding spheres. Engineering Computations 28 (7), 792–801.
URL http://search.proquest.com/docview/898410715?accountid=10598

Lee, T., Lakes, R. S., Lal, A., 2000. Resonant ultrasound spectroscopy for measurement of mechanical damping: Comparison with broadband viscoelastic spectroscopy. Review of Scientific Instruments 71 (7), 2855–2861.
URL http://link.aip.org/link/?RSI/71/2855/1

Lee, W., Cho, K., Jang, H., 2009. Molecular dynamics simulation of rolling friction using nanosize spheres. Tribology Letters 33, 37–43.

Logan, J. D., 2006. Applied Mathematics, 3rd Edition. Wiley-Interscience.

Lygeros, J., Ramponi, F., 2010. Lecture notes on linear system theory. Automatic Control Laboratory, ETH Zurich.
URL http://control.ee.ethz.ch/~ifalst/docs/Notes/LectureNotes.pdf

May, W. D., Morris, E. L., Atack, D., 1959. Rolling friction of a hard cylinder over a viscoelastic material. Journal of Applied Physics 30 (11), 1713–1724.

Menard, K. P., 2008. Dynamic Mechanical Analysis : A Practical Introduction. Taylor & Francis.

Morland, L. W., 1967. Exact solutions for rolling contact between viscoelastic cylinders. The Quarterly Journal of Mechanics and Applied Mathematics 20 (1), 73–106.

Morland, L. W., 1968. Rolling contact between dissimilar viscoelastic cylinders. The Quarterly Journal of Mechanics and Applied Mathematics 25 (4), 363–376.

Munisamy, R., Hills, D., Nowell, D., 1991. Brief note on the tractive rolling of dissimilar elastic cylinders. International Journal of Mechanical Sciences 33 (3), 225–228.

Nowell, D., Hills, D., 1988. Tractive rolling of dissimilar elastic cylinders. International Journal of Mechanical Sciences 30 (6), 427 – 439.
URL http://www.sciencedirect.com/science/article/pii/0020740388900161

Oden, J., Lin, T., 1986. On the general rolling contact problem for finite deformations of a viscoelastic cylinder. Computer Methods in Applied Mechanics and Engineering 57 (3), 297–367.

Oyadiji, S. O., 1996. Damping of vibrations of hollow beams using viscoelastic spheres. Proc. SPIE 2720, Smart Structures and Materials 1996: Passive Damping and Isolation, 89 (May 1).
URL http://dx.doi.org/10.1117/12.239078

Persson, B., 2010. Rolling friction for hard cylinder and sphere on viscoelastic solid. The European Physical Journal E Soft Matter 33 (4), 327–333.

Pöschel, T., Schwager, T., Brilliantov, N., 1999. Rolling friction of a hard cylinder on a viscous plane. The European Physical Journal B - Condensed Matter and Complex Systems 10, 169–174.

Qiu, X., 2006. Full two-dimensional model for rolling resistance: hard cylinder on viscoelastic foundation of finite thickness. Journal of Engineering Mechanics 132 (11), 1241–1251.

Qiu, X., 2009. Full two-dimensional model for rolling resistance. ii: Viscoelastic cylinders on rigid ground. Journal of Engineering Mechanics 135 (1), 20–30.

Rammohan Rao, B., Ganapathy, S., 1979. Linear time-varying systemsstate transition matrix. Electrical Engineers, Proceedings of the Institution of 126 (12), 1331–1335.

Scheibert, J., Prevost, A., Debrgeas, G., Katzav, E., Adda-Bedia, M., 2009. Stress field at a sliding frictional contact: Experiments and calculations. Journal of the Mechanics and Physics of Solids 57 (12), 1921 – 1933.
URL http://www.sciencedirect.com/science/article/pii/S0022509609001276

Subramaniam, D. R., Gee, D. J., King, M. R., 2013. Deformable cell-cell and cell-substrate interactions in semi-infinite domain. Journal of Biomechanics 46 (6), 1067.
URL http://search.proquest.com/docview/1319185610?accountid=10598

Tabor, D., 1952. Cv. the mechanism of rolling friction. Philosophical Magazine Series 7 43 (345), 1055–1059.

Tabor, D., 1955. The mechanism of rolling friction. ii. the elastic range. Proceedings of the Royal Society of London. Series A, Mathematical and Physical Sciences 229 (1177), 198–220.

Tsai, C., Lin, Y.-C., Chen, W.-S., Su, H., 2010. Tri-directional shaking table tests of vibration sensitive equipment with static dynamics interchangeable-ball pendulum system. Earthquake Engineering and Engineering Vibration 9 (1), 103–112.
URL http://dx.doi.org/10.1007/s11803-010-9009-4

Tschoegl, N., 1989. The phenomenological theory of linear viscoelastic behavior: an introduction. Springer-Verlag.

Wang, G., Knothe, K., 1993. Stress analysis for rolling contact between two viscoelastic cylinders. Journal of Applied Mechanics 60 (2), 310–317.

Wu, C.-W., Hwang, C.-K., 2008. A novel spherical wheel driven by omni wheels. In: Machine Learning and Cybernetics, 2008 International Conference on. Vol. 7. pp. 3800–3803.

Wu, C.-W., Qiu, Z.-W., Wang, Y.-H., Hsu, P.-H., Hwang, C.-K., 2011. Modeling of a spherical robot driven by omni wheels. In: Machine Learning and Cybernetics (ICMLC), 2011 International Conference on. Vol. 3. pp. 1256–1260.

Xu, G., Shao, J.-Y., 2008. Human neutrophil surface protrusion under a point load: location independence and viscoelasticity. American Journal of Physiology - Cell Physiology 295 (5), C1434–C1444.
URL http://ajpcell.physiology.org/content/295/5/C1434.abstract

Xu, Y., Yung, K. L., Ko, S. M., 2007. A classroom experiment to measure the speed-dependent coefficient of rolling friction. American Journal of Physics 75 (6), 571–574.
URL http://link.aip.org/link/?AJP/75/571/1

Yung, K., Xu, Y., 2003. Non-linear expressions for rolling friction of a soft ball on a hard plane. Nonlinear Dynamics 33 (1), 33–41.
URL http://dx.doi.org/10.1023/A%3A1025582521870

Yung, K. L., Xu, Y., Ng, H. P., 2007. Modelling method for studying solid conveying process in inclined plastication unit. Plastics, Rubber & Composites 36 (2), 56 – 61.
URL http://search.ebscohost.com.proxy.lib.duke.edu/login.aspx?direct=true&db=a9h&AN=24354167&site=ehost-live&scope=site

Zéhil, G.-P., Gavin, H. P., 2013a. Simple algorithms for solving steady-state frictional rolling contact problems in two and three dimensions. International Journal of Solids and Structures 50 (6), 843–852.
URL http://www.sciencedirect.com/science/article/pii/S0020768312004921

Zéhil, G.-P., Gavin, H. P., 2013b. Simplified approaches to viscoelastic rolling resistance. International Journal of Solids and Structures 50 (6), 853–862.
URL http://www.sciencedirect.com/science/article/pii/S002076831200409X

Zéhil, G.-P., Gavin, H. P., 2013c. Three-dimensional boundary element formulation of a viscoelastic layer of finite thickness applied to the rolling resistance of a rigid sphere. International Journal of Solids and Structures 50 (6), 833–842.
URL http://www.sciencedirect.com/science/article/pii/S002076831200491X

Zéhil, G.-P., Gavin, H. P., 2013d. Two and three-dimensional boundary element formulations of compressible isotropic, transversely isotropic and orthotropic viscoelastic layers of arbitrary thickness, applied to the rolling resistance of rigid cylinders and spheres. European Journal of Mechanics - A/Solids (under review).

Zheng, Q., Zhu, H., Yu, A., 2011. Finite element analysis of the rolling friction of a viscous particle on a rigid plane. Powder Technology 207 (13), 401 – 406.
URL http://www.sciencedirect.com/science/article/pii/S0032591010006182

Zhou, Y., Wright, B., Yang, R., Xu, B., Yu, A., 1999. Rolling friction in the dynamic simulation of sandpile formation. Physica A: Statistical Mechanics and its Applications 269 (24), 536 – 553.
URL http://www.sciencedirect.com/science/article/pii/S0378437199001831

Zienkiewicz, O. C., Taylor, R. L., Sep. 2005. The Finite Element Method for Solid and Structural Mechanics, 6th Edition. Butterworth-Heinemann.